nature biomedical engineering

Article

https://doi.org/10.1038/s41551-026-01667-x

DeepDrugDiscovery identifies blood–brain barrier permeable autophagy enhancers for Alzheimer's disease

Received: 4 April 2025

Accepted: 23 March 2026

Published online: 24 April 2026

Check for updates

Yu Dong[1,18], Xianglu Xiao[2,3,4,18], Xu-Xu Zhuang[1,18], Wenfan Wu[3,5,6,18], Zi-Ying Wang[1,7], Shuang Zhang[1,8], Jin-Tao Li[1], Ke Zhang[1], Wen-Yu Fu[1], Jun-Ming Chen[1], Shi Hang Xiong[1], Shenglong Deng[2,4], Krinos Li[2], Chao Ma[3], Wangzhen Jin[3], Xurui Jin[3], Qiwei Cai[3], Han-Ming Shen[9], Min Li[10], Huanxing Su[1], Jian-Bo Wan[1], Hua Yu[1], Defang Ouyang[1,11], Keqiang Ye[12], Evandro F. Fang[13,14], Chris Soon Heng Tan[8], Guang Yang[2,15,16,17], Zhangming Niu[3,4,15] ✉ & Jia-Hong Lu[1] ✉

Dysfunctional autophagy, a key cellular cleaning process, is a key driver of brain ageing and neurodegenerative diseases such as Alzheimer's disease (AD). However, developing effective treatments by enhancing autophagy has been challenging, as most known compounds act through the broad mTOR pathway, risking side effects, and few can effectively penetrate the brain. To address this, we developed DeepDrugDiscovery—a mechanism-aware, AI-powered screening platform incorporating ADMET and blood–brain barrier penetrability predictions. Here we show that this platform successfully identified novel, mTOR-independent autophagy enhancers, with two lead compounds demonstrating an ability to cross the blood–brain barrier, clear AD-related protein aggregates and restore memory function in worm and mouse AD models. By releasing DeepDrugDiscovery as an open-source, modular tool, we offer a user-friendly AI platform that enables customized therapeutic screening. Our work establishes a scalable, AI-driven pipeline that integrates cross-species validation to rapidly discover mechanism-based therapeutics for diseases with high unmet medical need.

Alzheimer's disease (AD), the most prevalent neurodegenerative disorder, affects over 35 million individuals worldwide[1,2]. Autophagy, an evolutionarily conserved cellular process in eukaryotic cells, is essential for cellular waste clearance and materials recycling[3]. This lysosome-dependent pathway degrades damaged and unnecessary subcellular components (such as organelles and misfolded proteins), maintaining homeostasis in the central nervous system (CNS). Accumulating evidence highlights a potential driving role of autophagic dysfunction in the pathogenesis and progression of neurodegenerative diseases, particularly in AD[4–7]. Recent studies have indicated that small-molecule autophagy inducers can exert neuroprotective effects by clearing abnormal protein aggregates in brain tissue, such as Aβ and hyperphosphorylated proteins, as well as by restoring mitochondrial function and energy metabolism[8,9]. The clinical translation of autophagy enhancers in AD remains challenging. Although most known autophagy enhancers act via mTOR-dependent pathways, their clinical translation has been limited[10–12]. Targeting mTOR-independent pathways presents a promising alternative with a potentially improved safety profile. However, advancing this strategy is hampered by two principal factors: the diversity of biological mechanisms available

A full list of affiliations appears at the end of the paper. ✉e-mail: zhangming@mindrank.ai; jiahonglu@um.edu.mo

for drug targeting and the inherent difficulty in achieving sufficient blood–brain barrier (BBB) penetration with such compounds[10,13,14].

The advent of artificial intelligence (AI) has ushered in a transformative era for traditional drug discovery paradigms. By leveraging advanced algorithms and computational power, AI offers substantial assistance across multiple critical stages, including large-scale virtual screening, lead compound optimization and the prediction of pharmacokinetic/pharmacodynamic properties. These capabilities represent a notable leap forward from conventional computer-aided drug design, delivering marked improvements in both the efficiency and predictive accuracy of the discovery pipeline[15,16]. Despite these substantial advances, a notable limitation persists: current AI-driven platforms, while powerful, largely remain constrained by virtual screening strategies predicated on single target structures or specific ligand frameworks. This approach may not be fully adequate for addressing complex pharmacological phenomena where the therapeutic effect arises from modulating broader, multi-faceted biological mechanisms rather than interacting with a single, well-defined protein target.

Therefore, developing novel methodologies capable of conducting large-scale virtual screening based not on specific molecular structures but on shared biological mechanisms represents a critical and open challenge. To tackle this challenge, we developed DeepDrugDiscovery (https://deepdrugdiscovery.mindrank.ai/), an AI-driven drug discovery platform that moves beyond traditional virtual screening by adopting a mechanism-centric approach. Instead of relying on the chemical structural similarity emphasized by conventional methods[17–19], the platform screens for mTOR-independent autophagy inducers by identifying shared biological mechanisms, thereby enabling the discovery of structurally diverse compounds that act on the same pathway. Furthermore, the platform integrates absorption, distribution, metabolism, excretion and toxicity (ADMET) properties and BBB permeability predictions into a unified workflow, allowing for efficient prioritization of candidate compounds from large-scale virtual screening to experimental validation. This end-to-end design avoids the challenges associated with multi-platform data transfer and accelerates the discovery process. Using this approach, we successfully identified two novel lead compounds. Both demonstrated the ability to induce autophagy, penetrate the BBB and exert neuroprotective effects in animal models of AD. This outcome validates the efficacy and accuracy of this highly integrated multi-module AI-driven platform for CNS drug discovery and expands the toolbox for next-generation AI-driven drug discovery.

Establishment of an AI-accelerated platform for screening of mTOR-independent autophagy enhancers

We developed a hybrid molecular representation approach for molecular modelling (Fig. 1a–c). This approach integrates a variational autoencoder with a gated recurrent unit-based feature fusion module to encode molecular fingerprints alongside one-dimensional (1D) and three-dimensional (3D) descriptors. Initially, we constructed a comprehensive and structurally diverse compound library tailored to our screening objectives. Commercially available compounds were collected, curated and standardized, resulting in a dataset of 1.16 million compounds with substantial chemical diversity (Morgan fingerprint diversity score, 0.881 ± 0.001; ring system diversity, 3.585 ± 0.015; chemical space coverage, 3.411 ± 0.007) (Extended Data Fig. 1a and Supplementary Table 1). The compound library was used as a pre-training dataset for the variational autoencoder molecular representation model, which transformed molecular structures into information-rich latent representations without requiring activity-labelled training data.

The molecular representation model architecture used a gated recurrent unit cell to integrate 2,048-bit Morgan fingerprints (ECFP4) with 19 1D and 3D descriptors, effectively capturing both structural patterns and molecular properties. The variational autoencoder learned to compress and reconstruct molecular features while preserving a well-regularized latent space (validation reconstruction loss, 0.033 per bit; Kullback–Leibler divergence, 0.05–0.07) (Extended Data Fig. 1c). This unsupervised learning approach enabled the model to discern meaningful chemical relationships within the molecular space. The resulting latent representations enabled the calculation of virtual screening scores between any compound and the reference set using a molecular attention mechanism (Fig. 1c,d).

A set of 50 mTOR-independent autophagy enhancers was systematically curated using the autophagy modulator scoring system[11,20] as reference compounds (Extended Data Fig. 1b and Supplementary Table 2). In the virtual screening workflow, the initial step was to generate embeddings for both the reference compounds and the compound library using the molecular representation models. Our graphics processing unit (GPU)-accelerated molecular attention mechanism rapidly computed scores between each library compound and the 50 reference enhancers, generating a 50 × 1,155,606 scoring matrix within seconds (Fig. 1e,f and Extended Data Fig. 2a). High-dimensional virtual screening was performed as a ranking-based prioritization rather than a hypothesis-testing analysis, and therefore did not involve multiple-comparison correction.

Using the ADMET Ranker platform for multi-tiered filtering (Fig. 1g), we refined the initial 6,834 hits that had surpassed a selection threshold of 0.65 (Fig. 2a,b). This threshold was determined based on previous validation studies and computational efficiency considerations, aiming to balance downstream screening tractability with the risk of prematurely excluding potentially active compounds[21–23]. First, physicochemical property scoring narrowed the pool to 3,068 candidates with favourable drug-like properties (Fig. 2c,d). Subsequent assessment of BBB permeability and drug-likeness identified 449 compounds with optimal CNS penetration potential (ADMET score ≥10) (Fig. 2e). Final computational filtering, involving molecular docking of candidate compounds against mTOR-related targets (FKBP12, mTOR kinase and the FKBP12–mTOR complex) and verification of commercial availability, yielded 15 top candidates for experimental validation (Fig. 2f).

Validation of candidate mTOR-independent autophagy enhancers

To assess the autophagy-modulating activity of selected compounds, we utilized the well-established mRFP-EGFP-LC3 tandem fluorescent reporter system[24]. In this assay, GFP fluorescence is quenched within acidic autolysosomes, while RFP remains stable, with RFP-only signals denoting mature, functional autolysosomes. We used a PC12 cell line stably expressing mRFP-EGFP-LC3B to evaluate the effects of 15 candidates on autophagy modulation. Following treatment, we quantified red (RFP^+) and yellow (RFP^+/GFP^+) puncta among experimental groups. All 15 compounds induced autophagy at a level comparable to that induced by our positive control Torin1 (Fig. 3a,b). The observed increase in red puncta indicates enhanced autophagic flux. Furthermore, immunoblotting for LC3-II and SQSTM1/p62 confirmed these findings, revealing modulation of these key autophagy markers (Fig. 3c,d).

To determine whether the autophagy-inducing capacity of the tested compounds was cell-type specific, we extended our analysis to N2a neuroblastoma cells, examining biochemical changes in LC3-II and SQSTM1/p62 levels. Consistent with the observations in PC12 cells, treatment with these compounds also modulated LC3-II and SQSTM1/p62 protein levels in N2a cells, although the effects were variable. Notably, while some drugs induced minimal changes in LC3-II, they significantly reduced SQSTM1/p62 levels (Fig. 3e–j). Further evaluation identified seven compounds, clevidipine, ombuin (Omb), 3′,4′,7-trimethoxyquercetin, salicylic acid, hydroxygenkwanin, 2-hydroxycinnamic acid (2-HCA) and riluzole, that significantly decreased SQSTM1/p62 levels (Fig. 4a and

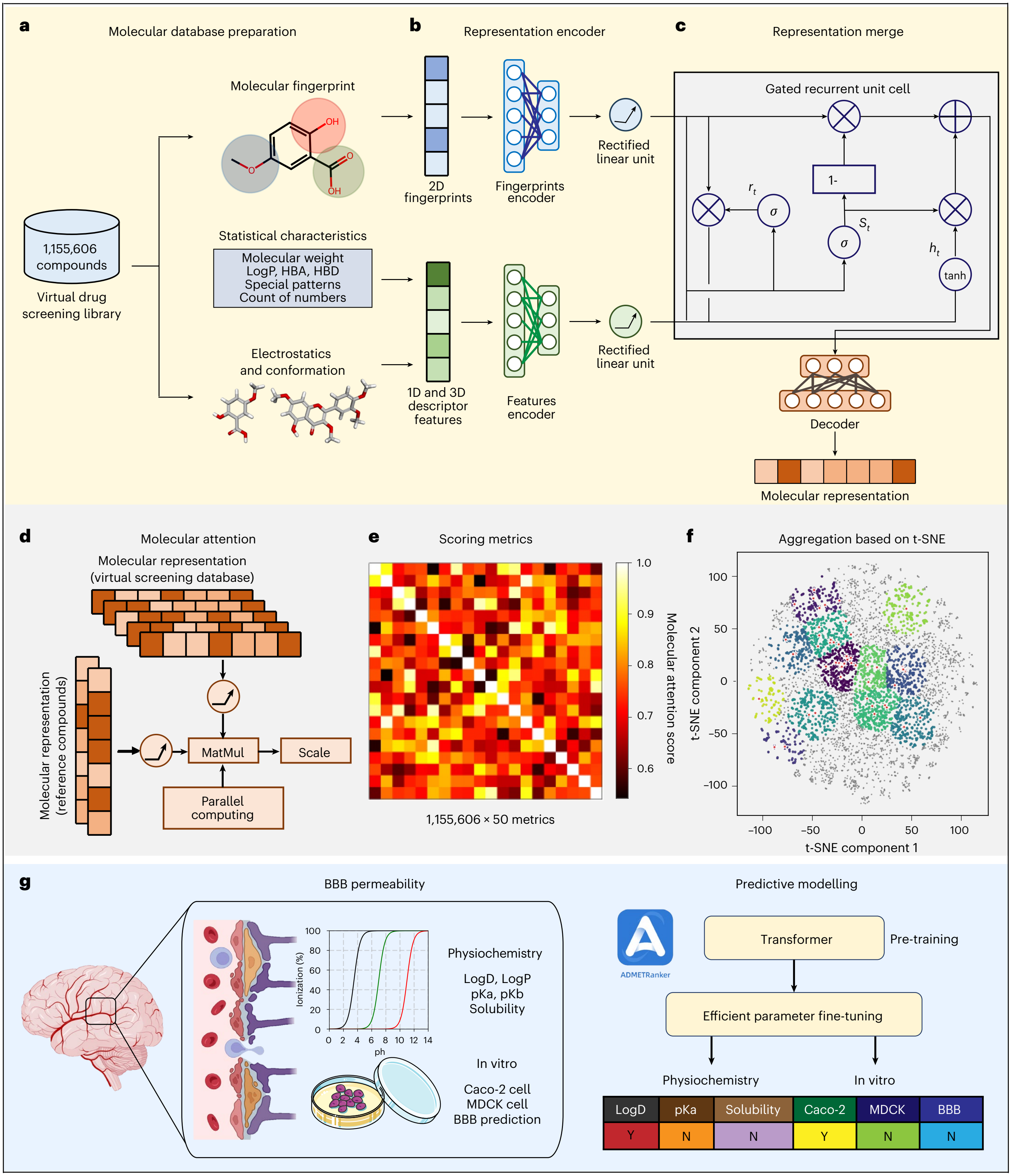

Fig. 1 | Workflow of the DeepDrugDiscovery for ligand-based virtual screening and predictive modelling. **a**, Molecular database preparation; HBA, hydrogen bond acceptor; HBD, hydrogen bond donor. **b**, Representation encoder. **c**, Representation merge. **d**, Molecular attention. **e**, Scoring metrics. **f**, Aggregation based on t-SNE. **g**, BBB permeability and ADMET predictions.

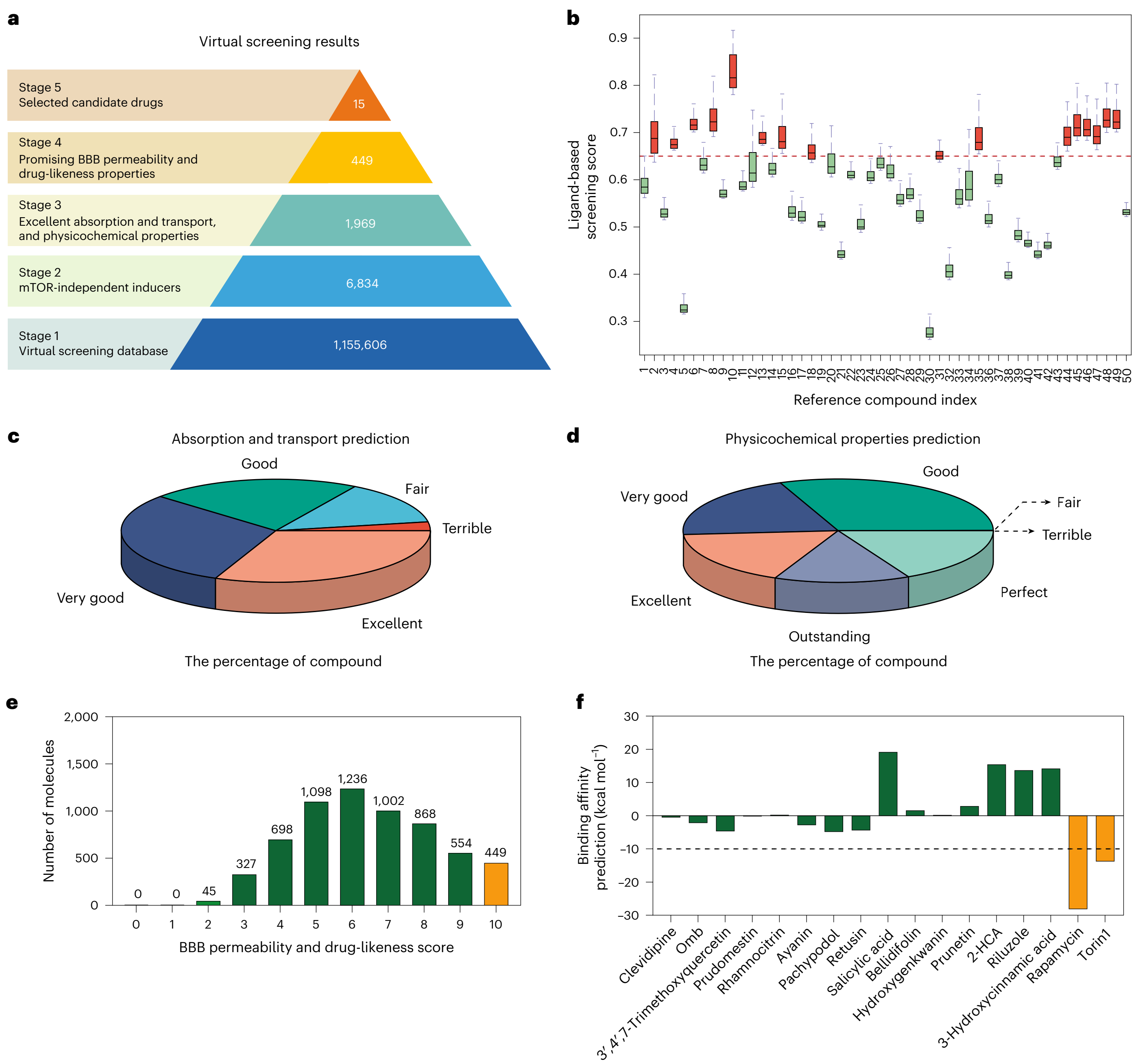

Fig. 2 | DeepDrugDiscovery screening results of BBB penetrating mTOR-independent autophagy inducers. a, Overall results of virtual screening. **b**, Top 500 ligand-based screening scores for 50 reference compounds. Box plots show the median (centre line) and interquartile range (box; 25th–75th percentiles). Whiskers extend to the most extreme values within 1.5× the interquartile range from the lower and upper quartiles. Outliers are not shown. The dashed red line indicates the screening score threshold (0.65). **c**–**e**, Predictions of compound properties: absorption and transport (**c**), key physicochemical parameters (**d**) and BBB permeability along with drug-likeness (**e**). **f**, Distribution of predicted binding free energies between candidate compounds and the mTOR protein.

Extended Data Fig. 3a,b). Moreover, these compounds increased the formation of mature autolysosome, as indicated by an increase in red puncta (Fig. 4b). To investigate the underlying mechanisms, we assessed the effects of these compounds on mTOR signalling and its downstream substrates. Unlike Torin1, a potent mTOR inhibitor that reduced phospho-mTOR (Ser2448), phospho-p70 S6 kinase (Ser371) and phospho-4E-BP1 (Thr37/46) levels, these seven candidates induced no significant changes (Fig. 4c), indicating that they induce autophagy independently of mTOR under the tested dose and experimental conditions.

Among the seven AI-nominated and experimentally validated mTOR-independent autophagy enhancers, we further evaluated their drug-like potential based on (i) the originality of their autophagy-inducing mechanisms of action, (ii) the novelty of their neuroprotective activities and (iii) the diversity of their chemical structures. This systematic evaluation led to the selection of four candidates, clevidipine, Omb, 2-HCA and 3′,4′,7-trimethoxyquercetin, for further development as potential treatments for AD (Extended Data Fig. 4a). To evaluate autophagic flux, we performed an LC3-II turnover assay, measuring LC3-II levels in the presence and absence of lysosomal inhibitors[25]. Co-treatment with bafilomycin A_1, alongside these four compounds and the positive control Torin1, significantly increased LC3-II and SQSTM1/p62 levels, confirming their ability to enhance autophagic flux (Fig. 4d,e and Extended Data Fig. 3c–f).

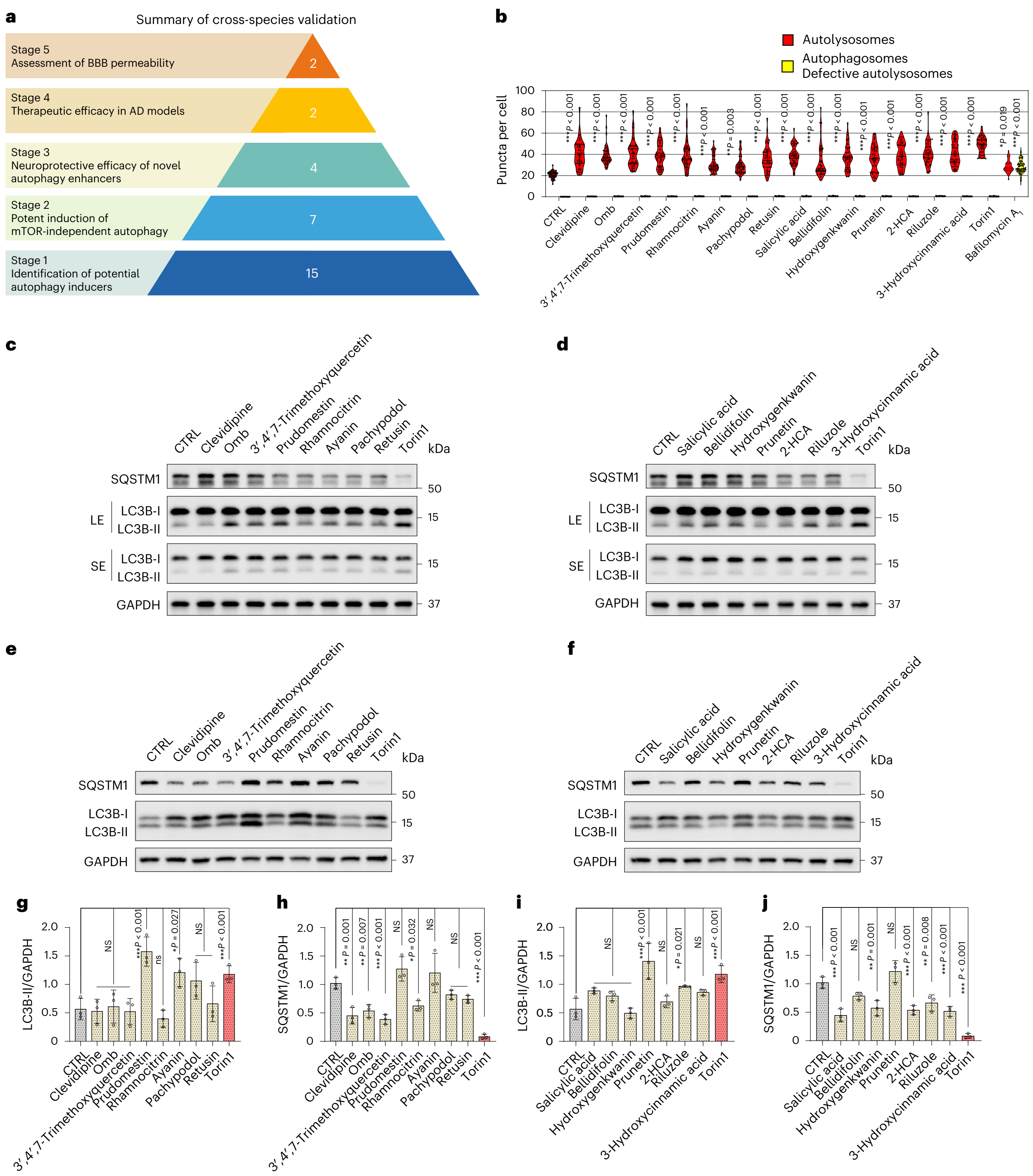

Fig. 3 | Validation of candidate compounds for autophagy modulation. **a**, Overall results of cross-species validation. **b**, Autophagic flux assay in PC12-mRFP-EGFP-LC3B cells. Cells were treated with indicated compounds (20 μM), Torin1 (1 μM) or bafilomycin A_1 (100 nM) for 12 h. Images were acquired using an Opera Phenix high-content imaging system. The average number of red and yellow dots per cell was quantified (cells ≥30, *n* = 3 independent biological replicates). **c**,**d**, Western blot (WB) analysis of LC3B-II and SQSTM1/p62 protein levels in PC12 cells treated with candidates (10 μM) or Torin1 (1 μM) for 24 h: clevidipine, ombuin (Omb), 3′,4′,7-trimethoxyquercetin, prudomestin, rhamnocitrin, ayanin, pachypodol, retusin (**c**) and salicylic acid, bellidifolin, hydroxygenkwanin, prunetin, 2-hydroxycinnamic acid (2-HCA), riluzole, 3-hydroxycinnamic acid (**d**); LE, long exposure; SE, short exposure. **e**,**f**, WB analysis of LC3B-II and SQSTM1/p62 protein levels in N2a cells under the same treatment conditions. **g**–**j**, Semi-quantification of **e**,**f** (*n* = 3 independent biological replicates). One-way analysis of variance (ANOVA) followed by Dunnett's multiple comparisons test (**b**,**g**–**j**). Quantitative data are shown as mean ± s.d. NS, not significant; *$P < 0.05$; **$P < 0.01$; ***$P < 0.001$. Original unprocessed WB gel data are in Source Data Fig. 3.

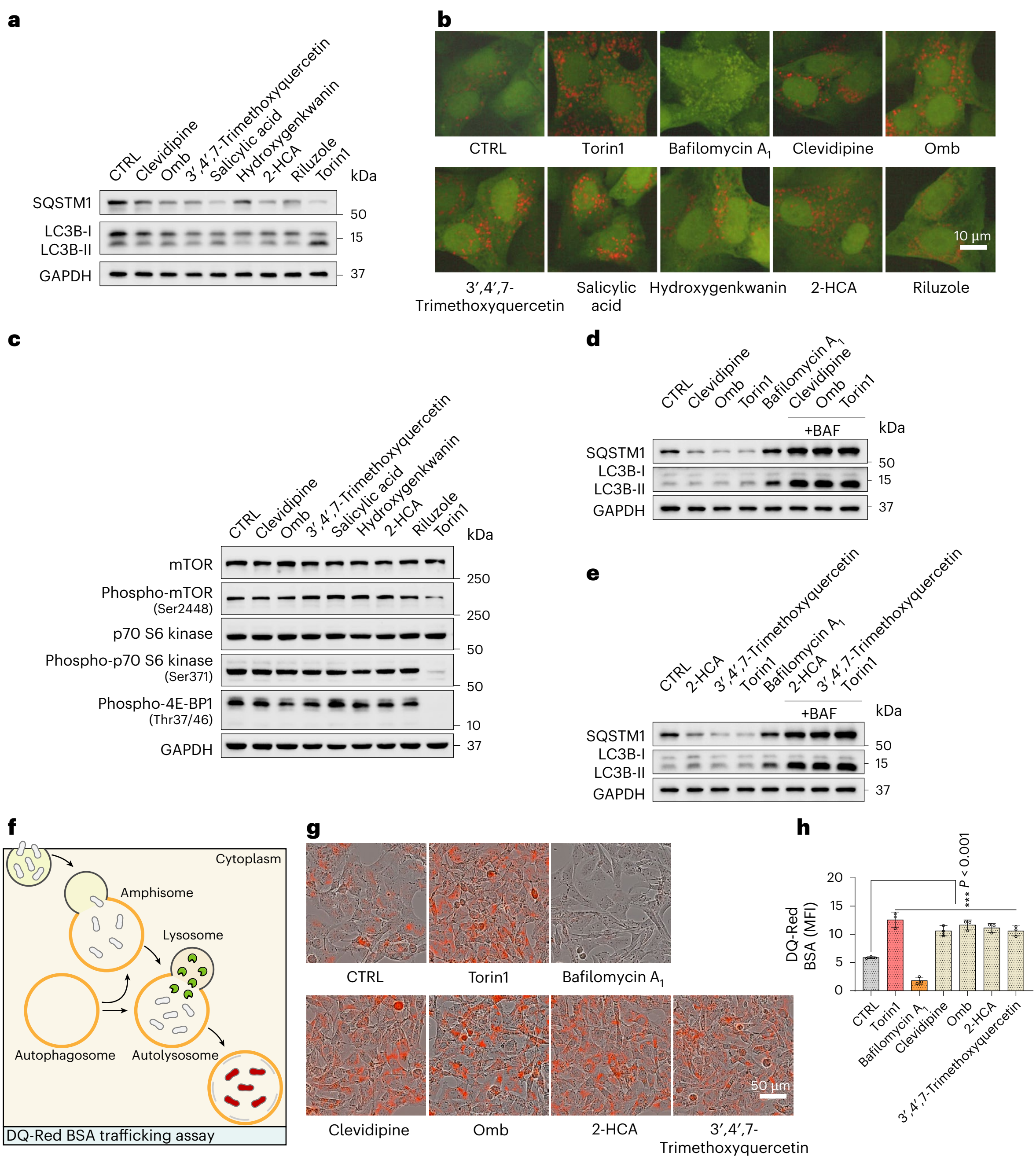

Fig. 4 | Characterization of candidate mTOR-independent autophagy enhancers. a, WB analysis of LC3B-II and SQSTM1/p62 protein levels in N2a cells treated with the indicated compounds (20 µM) or Torin1 (1 µM) for 24 h (*n* = 3 independent biological replicates). Statistical analyses are shown in Extended Data Fig. 3a,b. **b**, Autophagic flux assay in PC12-mRFP-EGFP-LC3B cells. Cells were treated with the indicated compounds (20 µM), Torin1 (1 µM) or bafilomycin A_1 (100 nM) for 12 h. Representative images acquired using an Opera Phenix system are shown (*n* = 3 independent biological replicates). **c**, WB analysis of mTOR and its downstream substrates protein levels in N2a cells treated with the indicated compounds (20 µM) or Torin1 (1 µM) for 6 h. **d**,**e**, WB analysis of LC3B-II and SQSTM1/p62 protein levels in N2a cells treated with the indicated compounds (20 µM) or Torin1 (1 µM) in the absence or presence of bafilomycin A_1 (100 nM) for 24 h (*n* = 3 independent biological replicates): clevidipine, ombuin (**d**) and 2-hydroxycinnamic acid, 3′,4′,7-trimethoxyquercetin (**e**). Statistical analyses are shown in Extended Data Fig. 3c,f. **f**–**h**, PC12 cells were pre-incubated with DQ-Red BSA for 0.5 h, followed by treatment with the indicated compounds (20 µM), Torin1 (1 µM) or bafilomycin A_1 (100 nM) for 4 h, and IncuCyte S3 live-cell analysis system was applied. Schematic diagram of DQ-Red BSA assay (**f**), the results of DQ-Red BSA assay (**g**), the mean fluorescence intensity (MFI) for each treatment in **g** was quantified and analysed (cells ≥30, *n* = 3 independent biological replicates) (**h**). One-way ANOVA followed by Dunnett's multiple comparisons test (**h**). Quantitative data are shown as mean ± s.d. NS, not significant; $*P < 0.05$; $**P < 0.01$; $***P < 0.001$. Original unprocessed WB gel data are in Source Data Fig. 4.

mTOR-independent autophagy enhancers promote autophagy and clear abnormal proteins in cellular models of AD

To robustly quantify autophagy-related cargo turnover and lysosomal proteolytic activity, we used the DQ-Red BSA assay[26,27]. Following cellular endocytosis, DQ-Red BSA traffics through early and late endosomes before merging with autophagosomes, which then fuse with lysosomes. In the acidic, hydrolase-rich lysosomal environment, DQ-Red BSA is cleaved, releasing detectable red fluorescent fragments (Fig. 4f). Treatment with clevidipine, Omb, 2-HCA and 3′,4′,7-trimethoxyquercetin

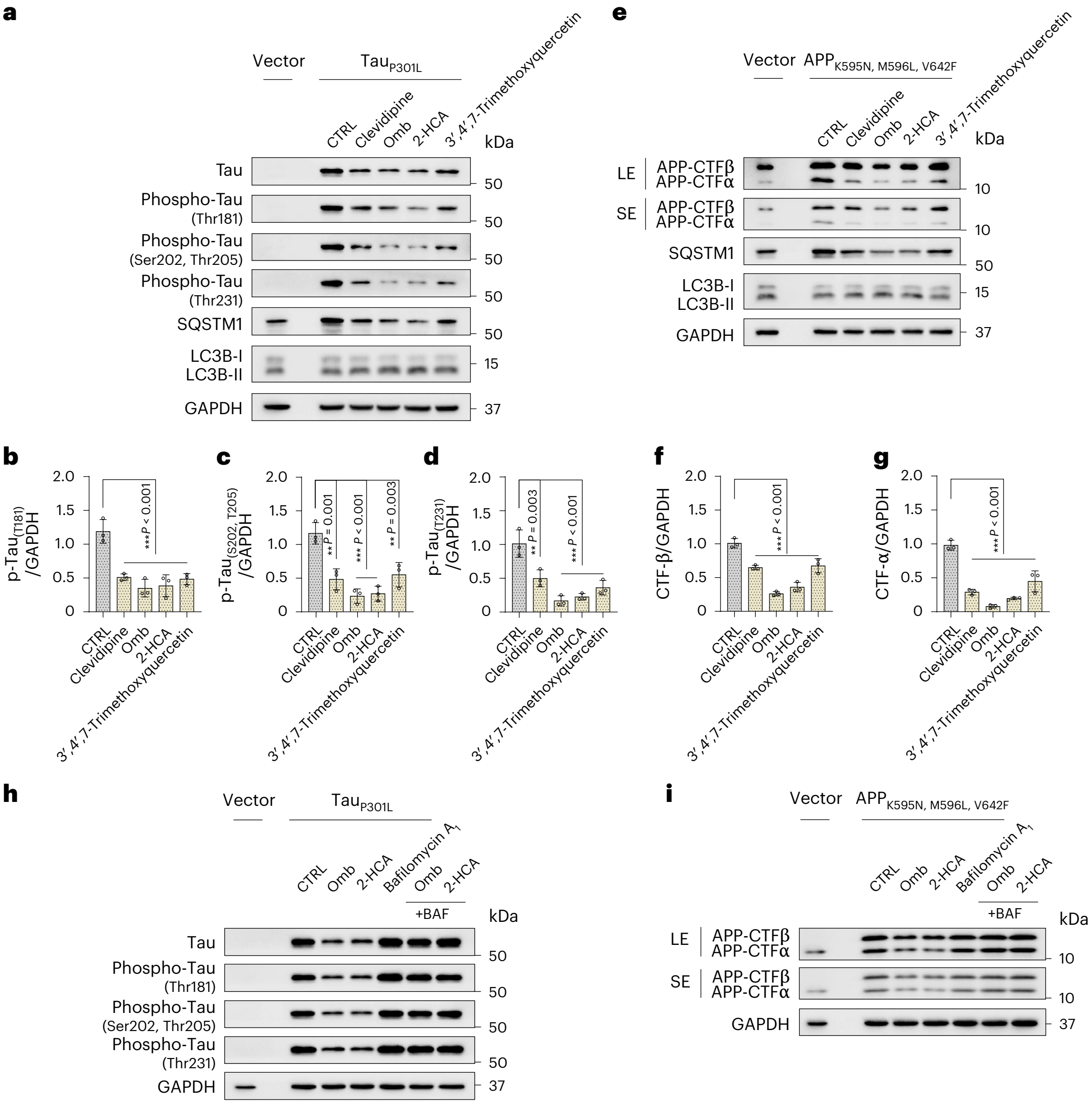

Fig. 5 | Clearance of AD-related pathological proteins by candidate compounds. a, WB analysis of total tau, phosphorylated tau (at multiple sites), LC3B-II and SQSTM1/p62 protein levels in PC12 cells stably expressing tau P301L treated with the indicated compounds (20 μM). **b**,**c**,**d**, Semi-quantification of **a** ($n = 3$ independent biological replicates). Statistical analyses are shown in Extended Data Fig. 4b–d. **e**, WB analysis of CTF-β, CTF-α, LC3B-II and SQSTM1/p62 protein levels in PC12 cells stably expressing APP KM595/596NL, V642F treated with the indicated compounds (20 μM). **f**,**g**, Semi-quantification of **e** ($n = 3$ independent biological replicates). Statistical analyses are shown in Extended Data Fig. 4e,f. **h**, WB analysis of total tau and phosphorylated tau (at multiple sites) protein levels in PC12 cells stably expressing tau P301L treated with Omb or 2-HCA at 20 μM in the absence or presence of bafilomycin A_1 (BAF; 100 nM) ($n = 3$ independent biological replicates). Statistical analyses are shown in Extended Data Fig. 5a–d. **i**, WB analysis of CTF-β and CTF-α protein levels in PC12 cells stably expressing APP K595N, M596L and V642F treated with the indicated compounds (20 μM) in the absence or presence of BAF (100 nM) ($n = 3$ independent biological replicates). Statistical analyses are shown in Extended Data Fig. 5e,f. One-way ANOVA followed by Dunnett's multiple comparisons test (**b**–**d**,**f**,**g**). Quantitative data are shown as mean ± s.d. NS, not significant; $*P < 0.05$; $**P < 0.01$; $***P < 0.001$. Original unprocessed WB gel data are in Source Data Fig. 5.

resulted in a marked increase in red fluorescence intensity, indicating enhanced autophagy induction and efficient substrate degradation in autolysosomes (Fig. 4g,h).

Genetic mutations in the genes encoding tau and amyloid precursor protein (APP) drive the formation of neurofibrillary tangles and amyloid plaques, recapitulating key pathological features of AD[28–30]. Given that pharmacologically induced autophagy can attenuate tau pathology and Aβ accumulation, autophagy enhancement represents a promising therapeutic strategy for AD[23,31,32]. In this study, we assessed four compounds, clevidipine, Omb, 2-HCA and 3′,4′,7-trimethoxyquercetin, in cell lines overexpressing mutant tau (P301L) or APP (K595N, M596L and V642F). Treatment with these compounds significantly reduced the levels of a series of key p-tau sites (Thr181, Ser202, Thr205 and Thr231) (Fig. 5a–d) and decreased levels of APP cleavage products (CTF-β and CTF-α) (Fig. 5e–g). Furthermore, treatment mildly elevated LC3 while markedly decreasing SQSTM1/p62 levels (Fig. 5a,e and Extended Data Fig. 4b–f). Collectively, these experiments identified Omb and 2-HCA as exhibiting the most potent therapeutic effects.

We next investigated whether Omb and 2-HCA promoted the degradation of hyperphosphorylated tau and APP-derived CTF-β/CTF-α via an autophagosome–lysosome-dependent pathway. To address this, we utilized SAR405 and bafilomycin A_1, two well-established autophagy inhibitors targeting early and late stages, respectively[33,34]. Co-treatment with either inhibitor blocked the autophagic flux induced by Omb and 2-HCA (Extended Data Fig. 4g), as well as the clearance of

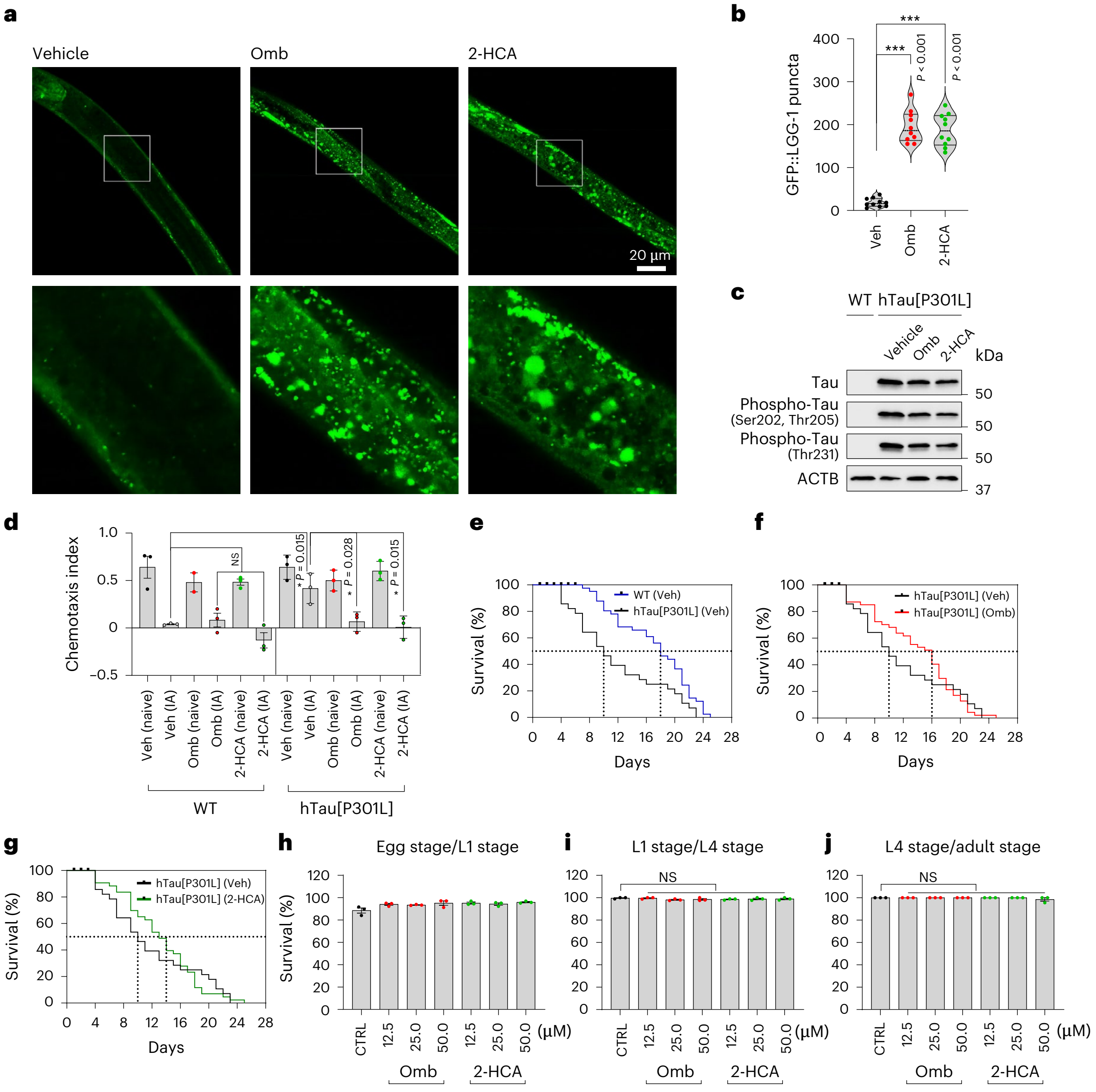

Fig. 6 | Omb and 2-HCA regulate autophagy and exhibit neuroprotective effects in the *C. elegans* model of AD. a, Analysis of autophagy activity in transgenic nematodes expressing GFP::LGG-1 treated with Omb or 2-HCA at 50 µM. Fluorescence images were captured using a laser scanning confocal microscope. **b**, The average number of green dots of **a** was quantified ($n = 10$ nematodes per group). Veh, vehicle; WT, wild type. **c**, WB analysis of total tau and phosphorylated tau (at multiple sites) protein levels in N2 and transgenic nematodes expressing hTau[P301L] (CK12) treated with Omb or 2-HCA at 50 µM. For sample preparation, >200 nematodes were pooled per group. **d**, Analysis of memory in N2 and CK12 treated with Omb or 2-HCA at 50 µM ($n = 3$ independent biological replicates). One-way ANOVA followed by Tukey's or Dunnett's multiple comparisons test (**d**). **e**–**g**, Analysis of lifespan in N2 and CK12 treated with Omb or 2-HCA at 50 µM: WT (Veh) vs hTau[P301L] (Veh) (**e**), hTau[P301L] (Veh) vs hTau[P301L] (Omb) (**f**) and hTau[P301L] (Veh) vs hTau[P301L] (2-HCA) (**g**). **h**–**j**, Analysis of toxicity from egg hatching, development to L4 stage and time to reach adulthood in N2 nematodes treated with Omb or 2-HCA at 12.5 µM, 25 µM and 50 µM ($n = 3$ independent biological replicates): from the egg stage to L1 stage (**h**), from L1 stage to L4 stage (**i**) and from L4 stage to adult stage (**j**). One-way ANOVA followed by Dunnett's multiple comparisons test (**b**,**i**,**j**). Quantitative data are shown as mean ± s.d. NS, not significant; $^{*}P < 0.05$; $^{**}P < 0.01$; $^{***}P < 0.001$. Original unprocessed WB gel data are in Source Data Fig. 6.

hyperphosphorylated tau (Fig. 5h and Extended Data Fig. 5a–d,g,i–l) and CTF-β/CTF-α fragments (Fig. 5i and Extended Data Fig. 5e,f,h,m,n). In addition, we confirmed that physiologically relevant concentration of Omb could still increase autophagic flux (Extended Data Fig. 4h,i). These findings confirmed that the observed clearance effects were dependent on the autophagic pathway.

Omb and 2-HCA enhance autophagy and exert neuroprotective effects in a *C. elegans* model of AD

To assess compound effects on autophagy in *Caenorhabditis elegans* (*C. elegans*), we used a GFP::LGG1 reporter strain, in which the formation of GFP-positive puncta (LGG1 is the *C. elegans* orthologue of mammalian LC3/GABARAP proteins) indicates autophagic activity. Treatment with Omb (50 µM) and 2-HCA (50 µM) significantly increased the number of GFP::LGG1 puncta compared with untreated controls (Fig. 6a,b), indicating increased autophagic flux. We next evaluated the effects of the two lead compounds in *C. elegans* models expressing human tau P301L, which recapitulate key features of AD. This model system has been used to successfully screen drug candidates against AD, and some of the screened positive compounds now in clinical trials[23,32,35]. Immunoblotting assays revealed that both compounds effectively reduced mutant tau protein levels (Fig. 6c), confirming that compound-induced autophagy led to degradation of the aggregation-prone tau variant.

The chemotaxis assay, which quantifies worm movement towards attractants, offers a reliable and sensitive behavioural measure of learning and memory deficits in these organisms[36]. In this paradigm, starvation was used as an aversive stimulus with isoamyl alcohol as a 'cue' linked to 'no food'. Wild-type worms, preconditioned with isoamyl alcohol and subsequently re-exposed, exhibited learned aversion by moving away from the stimulus source. By contrast, tau P301L transgenic worms showed impaired learning and memory, failing to exhibit the anticipated aversion even after preconditioning, recapitulating cognitive deficits observed in neurodegenerative diseases. Notably, Omb (50 μM) and 2-HCA (50 μM) significantly improved the chemotaxis index in tau transgenic worms (Fig. 6d), indicating restored memory function.

Finally, we assessed the effect of compound treatment on lifespan. Consistent with previous reports[23] and analogous to reduced survival in patients with AD[37,38], tau P301L transgenic worms exhibited a shortened median lifespan compared with wild-type animals (Fig. 6e). This shortened lifespan reflects the deleterious effects of pathological tau expression, serving as a biological readout of tauopathy-related impairment. Treatment with Omb (50 μM) or 2-HCA (50 μM) significantly extended the median lifespan of tau transgenic worms by 6 and 4 days, respectively (Fig. 6f,g), supporting the conclusion that these compounds confer neuroprotection and mitigate tau-induced toxicity. Finally, we confirmed that Omb and 2-HCA did not show any detectable side effects or developmental toxicity, as assessed through egg hatching, progression to the L4 larval stage and timing of adulthood (Fig. 6h–j).

Omb and 2-HCA stimulate autophagy, improve cognitive function and clear abnormal protein aggregates in 3×Tg-AD mice

The 3×Tg-AD mouse model, which overexpresses mutant APP, tau and presenilin 1, reproduces both Aβ and tau pathological features[39,40]. We assessed the neuroprotective effects of Omb and 2-HCA in 3×Tg-AD mice by analysing changes in spatial memory using the Morris water maze (Fig. 7a,b). Over four training days, wild-type mice exhibited progressive learning, reflected in reduced latency to find the hidden platform (Fig. 7c). By contrast, untreated 3×Tg-AD mice, exhibiting impaired memory and learning, showed no significant reduction in latency. Treatment with Omb (10 mg kg^{-1} per day) or 2-HCA (10 mg kg^{-1} per day) for 2 months beginning at age 16 months ameliorated these deficits (Fig. 7c). On day 5, with the platform removed, drug-treated 3×Tg-AD mice showed increased crossings over the former platform location and spent more time and distance in the target quadrant (Fig. 7d–g), indicating improved spatial memory in this AD model.

Short-term learning and memory were further assessed using the Y-maze and Novel Object Recognition tests (Fig. 7h,j). Compared with wild-type controls, untreated 3×Tg-AD mice showed significantly impaired performance in both assays (Fig. 7i,k), consistent with their characteristic cognitive impairments. Following treatment with Omb or 2-HCA, 3×Tg-AD mice exhibited substantial improvement in the Y-maze, as evidenced by increased spontaneous alternation behaviour, a marker of enhanced working memory (Fig. 7i). In this test, although the effect of 2-HCA on recognition memory did not reach statistical significance, a trend towards improvement was observed for both compounds (Fig. 7k).

After behavioural testing, hippocampal tissues from 3×Tg-AD mice were collected and cryosectioned. Immunostaining was performed on the vulnerable CA1 region[41,42] to assess the deposition of phosphorylated tau (p-Thr217) and Aβ (detected with the 4G8 antibody) (Fig. 7a). Omb and 2-HCA substantially reduced phosphorylated tau and Aβ levels in the CA1 region (Fig. 8a,b and Extended Data Fig. 6a,b). Western blot analysis further confirmed significant reductions in total tau, its key phosphorylated isoforms and APP cleavage products (CTF-β and CTF-α) (Fig. 8c–j and Extended Data Fig. 6c). In addition, both compounds increased LC3-II levels and decreased SQSTM1/p62 levels (Fig. 8e,k and Extended Data Fig. 6d), consistent with enhanced autophagic flux. The administered doses of Omb and 2-HCA appeared to be well tolerated, as evidenced by the absence of significant body weight changes (Extended Data Fig. 6e).

Omb and 2-HCA exhibit BBB penetration

The BBB is a highly selective semipermeable interface that protects the CNS from harmful substances in the circulation while also presenting a major obstacle for the delivery of therapeutic agents targeting the brain. Thus, the ability of a compound to cross the BBB is a crucial factor in the development of treatments for CNS disorders. To evaluate BBB penetration, we measured the brain penetration profiles of Omb and 2-HCA in young mice following intravenous (tail vein) injection at a dose of 10 mg kg^{-1}, consistent with the dosage used in our therapeutic efficacy studies in AD mouse models. Concentrations of each compound were quantified in brain tissue, plasma and cerebrospinal fluid at 0.5 h, 1 h and 2 h post-administration. The results demonstrated that Omb was detectable in brain tissue at both 0.5 h and 1 h, reaching a peak concentration of 516.00 ± 138.70 ng g^{-1} at 0.5 h post-injection. This was accompanied by a relatively high brain-to-plasma ratio (>10), confirming its favourable BBB penetration capability. Although the brain concentration of 2-HCA was low (7.07 ± 0.40 ng g^{-1}) and only transiently detectable (at 0.5 h), its notable in vivo efficacy indicates that its neuroprotective effects may be mediated through alternative mechanisms. These could include facilitated accumulation in the CNS via AD-associated BBB impairment[43,44] and/or carrier-mediated transport[45,46] (Table 1).

Predicted molecular mechanisms underlying autophagy induction by Omb and 2-HCA

To explore the molecular mechanisms by which Omb and 2-HCA promote mTOR-independent autophagy, we used an integrated, multi-tiered experimental strategy (Extended Data Fig. 7a). Initially, thermal proteome profiling was applied to identify potential binding proteins for both compounds[47] (Extended Data Fig. 7b,c). We then used the Enrichr tool to perform pathway enrichment analysis on the predicted target proteins of Omb and 2-HCA ($P < 0.05$, $\log_2 FC > 0.5$)[48,49]. This integrated analysis identified Pip4k2a and Mtmr1 as the most promising targets for Omb, and Ikbkb and Mapk8ip3 as primary candidates for 2-HCA, based on the strong enrichment of these proteins with autophagy-related pathways (that is, inositol phosphate metabolism and MAPK signalling) (Extended Data Fig. 8a–d and Supplementary Tables 7–10).

Protein–protein interaction analysis via the STRING database[50] suggested that Omb may modulate phosphoinositide metabolism through Pip4k2a and Mtmr1, potentially altering PI3P and PI5P levels and thereby regulating the PI3KC3-C1 complex, a key regulator of autophagosome nucleation and elongation (Extended Data Figs. 7d and 8e,g). By contrast, 2-HCA likely acts through a different mechanism, potentially involving the IKK–JNK1–Bcl-2 axis, which may regulate Bcl-2 phosphorylation and subsequent release of Beclin1, modulating assembly of the autophagy-initiation complex PI3KC3-C1 (Extended Data Figs. 7e and 8f,h).

Structurally, co-folding analyses using Boltz-2[51] indicated strong binding potential between Omb and both Pip4k2a and Mtmr1, while 2-HCA exhibited preferential binding capability with Ikbkb (Extended Data Figs. 7f,g and 8i,j and Supplementary Table 11). Molecular dynamics simulations of the Omb–Pip4k2a, Omb–Mtmr1 and 2-HCA–Ikbkb complexes revealed that all three systems maintained relatively stable conformations throughout the simulation trajectories, with key dynamic parameters supporting their structural integrity (Extended Data Fig. 9).

Collectively, these data support a hypothetical model in which both Omb and 2-HCA bypass canonical mTOR-dependent signalling to directly promote autophagosome nucleation and elongation, albeit

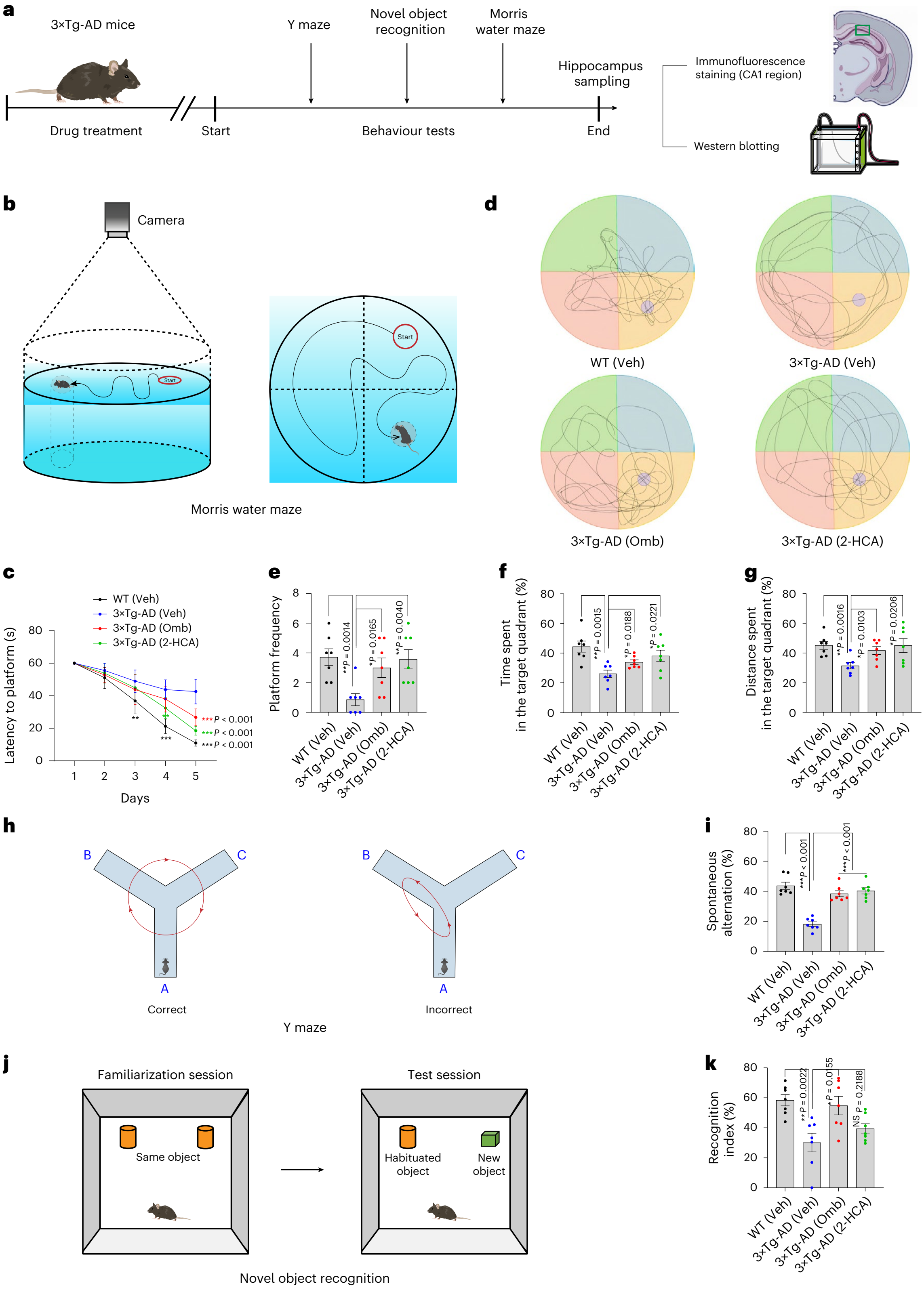

Fig. 7 | Omb and 2-HCA improve cognitive dysfunction in the 3×Tg-AD mouse model. a, Experimental timeline. The 3×Tg-AD mice were treated with Omb or 2-HCA at a dose of 10 mg kg^{-1} per day for 2 months via intraperitoneal injection. Upon completion of behavioural testing, mice were euthanized and transcardially perfused. Hippocampal tissue was collected for immunofluorescence and WB analyses. **b**–**g**, Performance in the Morris water maze test ($n = 7$ mice per group): schematic diagram of the Morris water maze (**b**), analysis of latency to platform (**c**,**d**), analysis of platform frequency (**e**), analysis of time spent in the target quadrant (**f**) and analysis of distance spent in the target quadrant (**g**). **h**–**k**, Performance in the Y maze and Novel object recognition ($n = 7$ mice per group): schematic diagram of the Y maze and Novel object recognition (**h**,**j**), analysis spontaneous alternation (**i**) and analysis of recognition index (**k**). Two-way ANOVA followed by Tukey's multiple comparisons test (**c**). One-way ANOVA followed by Dunnett's multiple comparisons test (**e**–**g**,**i**,**k**). Quantitative data are shown as mean ± s.d. NS, not significant; $^{*}P < 0.05$; $^{**}P < 0.01$; $^{***}P < 0.001$.

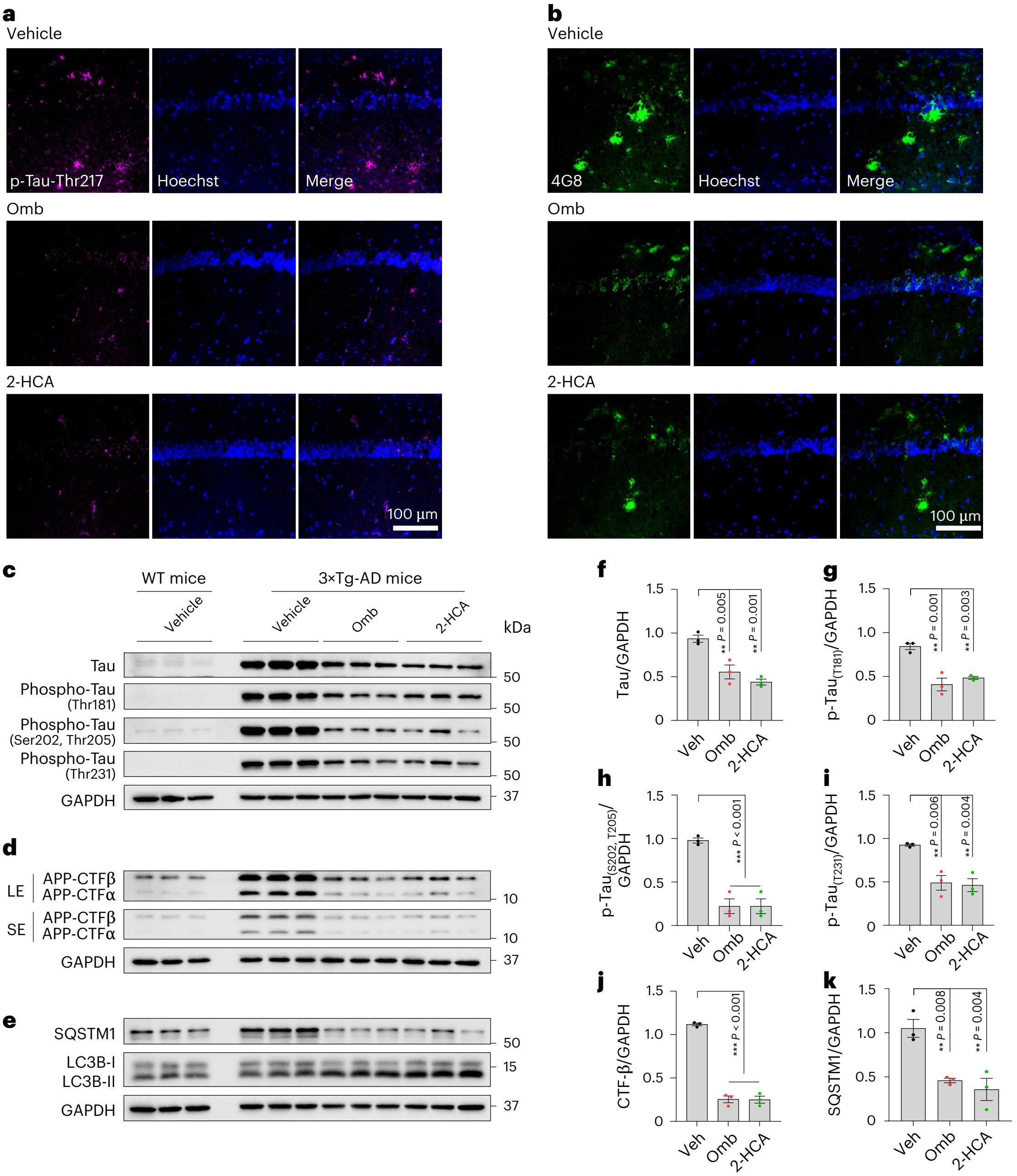

Fig. 8 | Omb and 2-HCA demonstrate the ability to clear abnormal protein aggregates in the 3×Tg-AD mouse model. a,**b**, Representative immunofluorescence images of phosphorylated tau (p-Thr217) (pseudo-coloured in magenta) (**a**) and Aβ (**b**) in the hippocampal CA1 region ($n = 7$ mice per group). **c**–**e**, WB analysis of total tau, phosphorylated tau (at multiple sites) (**c**), CTF-β, CTF-α (**d**), LC3B-II and SQSTM1/p62 (**e**) protein levels in mouse hippocampal tissues. **f**–**k**, Semi-quantification of **c**–**e** ($n = 3$ mice per group). One-way ANOVA followed by Dunnett's multiple comparisons test (**f**–**k**). Quantitative data are shown as mean ± s.d. NS, not significant; $^{*}P < 0.05$; $^{**}P < 0.01$; $^{***}P < 0.001$. Original unprocessed WB gel data are in Source Data Fig. 8.

through distinct molecular targets and pathways. While these proposed mechanisms are inferred from integrated computational and proteomic data and provide a testable framework for understanding compound action, they require further validation through targeted experimental approaches.

Discussion

Recent advances in AI have markedly improved the efficiency of machine learning and deep learning-based drug screening, offering substantially higher throughput than traditional experimental methods[52,53]. Despite this progress, AI-driven drug discovery is still an evolving field, facing persistent challenges in predictive accuracy, model stability and operational efficiency. In our earlier work, we developed an AI platform to identify mitophagy modulators for neurodegenerative diseases[23], but its utility was limited by a small compound library (~3,000 molecules), lack of capability for mechanism- or pathway-driven screening, and the absence of integrated BBB permeability evaluation.

To build upon this foundation and overcome these limitations, we developed DeepDrugDiscovery, a novel platform designed to identify mTOR-independent autophagy inducers with favourable BBB penetration. The key features of DeepDrugDiscovery include (1) a mechanism-driven screening paradigm that differs from conventional structure- or ligand-based approaches; (2) higher screening efficiency, hit rate and predictive accuracy compared with existing virtual screening tools[54–60] (Extended Data Fig. 2a and Supplementary Tables 3–6); (3) integrated ADMET prediction capabilities relative to mainstream

Table 1 | Pharmacokinetics study of Omb and 2-HCA

	Time (h)	Omb	2-HCA
Brain concentration (ng g^{-1})	0.5	516.00±138.70	7.07±0.40
	1	45.23±4.88	BLLOQ
	2	BLLOQ	BLLOQ
Plasma concentration (ng ml^{-1})	0.5	32.07±20.85	382.23±90.73
	1	2.29±0.34	29.63±15.45
	2	BLLOQ	2.71±0.80
Cerebrospinal fluid concentration (ng ml^{-1})	0.5	BLLOQ	BLLOQ
	1	BLLOQ	BLLOQ
	2	BLLOQ	BLLOQ

Data are mean ± s.d. BLLOQ, below the lower limit of quantitation (LLOQ). Brain LLOQ (ng g^{-1}), 5.00; plasma LLOQ (ng ml^{-1}), 2.00; cerebrospinal fluid LLOQ (ng ml^{-1}), 6.00

platforms[61–64] (Extended Data Fig. 2b–e), a critical feature that aids in the selection of drug-like candidates; and (4) comprehensive cross-species experimental validation, bridging AI-based prediction and wet-lab confirmation to ultimately establish biological relevance.

Despite being a promising therapeutic strategy for neurodegenerative diseases for over two decades, no autophagy-targeting drug has been approved for AD treatment so far. Numerous challenges hinder the translation of this approach, including the complexity of autophagy regulation in the brain and the lack of effective biomarkers to monitor autophagic activity in vivo. Major obstacles include the side effects associated with classical mTOR-dependent agents and the difficulty in developing BBB-permeable autophagy enhancers. In this study, we identified and validated two mTOR-independent, BBB-permeable autophagy enhancers that exhibit neuroprotective effects in cellular, *C. elegans* and mouse models of AD, providing candidates for future therapeutic development.

Nevertheless, this study has certain limitations, which also represent opportunities for future research. Methodological limitations currently restrict direct measurement of autophagic flux in brain tissue; future studies could utilize tools such as mRFP-GFP-LC3 transgenic mice to monitor autophagic activity within specific neural populations[65]. Moreover, the therapeutic efficacy of these compounds has thus far been evaluated in only a limited range of preclinical models. Translation of these preclinical findings into clinical applications will require comprehensive safety assessments and rigorous clinical trials to conclusively demonstrate efficacy and address potential concerns, including excessive autophagy induction or off-target effects[66]. While DeepDrugDiscovery maintains substantial enrichment under similarity-stratified and scaffold-split out-of-distribution evaluations, extending such performance to truly novel chemical space remains intrinsically challenging owing to sparse data support and the frequent requirement for de novo synthesis and optimization. Consequently, predictions in extreme novelty regimes should be interpreted as hypothesis-generating and pursued in close coordination with iterative experimental validation.

In addition, natural products pose both a challenge and an opportunity in target discovery owing to their polypharmacology—that is, their ability to engage multiple targets simultaneously[67,68]. While this multi-target engagement often underlies their therapeutic efficacy, it also complicates the precise elucidation of their primary mechanisms of action. To address this challenge, we used an integrated multi-layered strategy combining thermal proteome profiling, bioinformatics, co-folding analysis and molecular dynamics simulations to rapidly generate target hypotheses and accelerate deconvolution of candidate compound targets. However, these predictions remain largely unvalidated and function primarily as prioritization tools; definitive target confirmation requires systematic downstream experimental validation.

Furthermore, the robustness and generalizability of the DeepDrugDiscovery platform could be further enhanced through future computational developments, such as (i) improving BBB permeability prediction models, (ii) implementing uncertainty-based active learning to iteratively refine predictions with new experimental data and (iii) fine-tuning the variational autoencoder as more pathway-specific datasets become available.

Methods

Identification of mTOR-independent autophagy enhancers using the autophagy modulator scoring system

To identify reference mTOR-independent autophagy enhancers, we implemented a rigorous, multi-step strategy. First, we compiled a comprehensive database of pharmacological studies reporting autophagy enhancers. We then applied the autophagy modulator scoring system to evaluate the methodological rigour of each study. For each candidate molecule, we performed an exhaustive literature review using 'mTOR' as a keyword to confirm the absence of reported mTOR pathway modulation. In addition, to minimize the risk of overlooking relevant compounds, we manually curated autophagy-related review articles to identify and confirm additional mTOR-independent candidates. This multi-faceted approach ensured a meticulous and scientifically robust selection for reference compounds, thereby establishing the foundation for our subsequent AI-driven screening.

Ligand-based virtual screening process

The ligand-based virtual screening workflow began with the assembly of a high-quality library of 1,155,606 compounds, which served as the training dataset for a variational autoencoder to perform unsupervised molecular representation learning. The trained variational autoencoder generated latent embeddings for all library compounds and a curated reference set of validated mTOR-independent autophagy enhancers. Using a GPU-accelerated scoring framework, we identified 6,834 compounds with similarity scores exceeding 0.65 relative to the reference enhancers. These initial hits underwent multi-tiered pharmacokinetic evaluation using our ADMET Ranker, prioritizing BBB permeability and overall drug-likeness, which reduced the candidate pool to 449 compounds. A final computational filter, incorporating molecular docking against mTOR binding sites and verification of CAS number availability, yielded 15 top candidates, which were advanced for experimental validation.

For the specific screening process, a compound library comprising 1.16 million molecules was curated from established commercial suppliers, including MedChemExpress, TSBiochem and other reputable vendors, and is publicly accessible via Figshare (https://figshare.com/articles/dataset/Compound_Library_for_DeepDrugDiscovery_platform/31123354). This strategic sourcing ensures the ready availability of identified hits, circumventing synthesis bottlenecks and facilitating a seamless transition from computational prediction to experimental validation. For computational analysis, all library compounds were converted into Simplified Molecular Input Line Entry System (SMILES) format. This conversion involved three critical steps to ensure the accuracy and usability of SMILES representations: (1) removal of invalid and duplicate SMILES notations, (2) desalting of compounds and (3) normalization of SMILES notations (details are provided in the Supplementary Methods). Comprehensive diversity analysis confirmed broad and unbiased coverage of chemical space, evidenced by high Morgan fingerprint diversity (0.881 ± 0.001), substantial scaffold variety (ring system diversity 3.585 ± 0.015) and robust chemical space coverage (3.411 ± 0.007) (Supplementary Table 1). Physicochemical profiling further revealed favourable drug-like properties, with molecular weights ranging from 200 Da to 600 Da, balanced lipophilicity (LogP centred around 3), low hydrogen bond donor counts (0–4) and appropriate topological polar surface area distributions (Extended Data Fig. 1a).

To enhance molecular representation generation, we trained a variational autoencoder model using a tailored hybrid architecture designed for unsupervised molecular representation learning. The model takes 2,048-bit Morgan fingerprints (ECFP4) as the primary input to capture structural features via circular atom neighbourhoods. These are supplemented by 19 one- and two-dimensional molecular descriptors, which were discretized using a uniform KBinsDiscretizer before encoding. The encoder network consists of a configurable multi-layer stack incorporating batch normalization, rectified linear unit activation and dropout applied after each layer. Molecular fingerprints and auxiliary descriptors undergo separate linear transformations before being integrated via a gated recurrent unit cell, which effectively captures interdependencies between structural and physicochemical properties. The fused representation is then processed through the encoder stack to generate the parameters of the latent distribution. The decoder network transforms sampled latent vectors to reconstruct the fingerprint space using a sigmoid-activated output layer. Details of the model architecture are provided in the Supplementary Methods.

The variational autoencoder was trained in a fully unsupervised manner on a comprehensive compound library of 1.16 million molecules, using an 80/20 train–validation split to ensure robust learning and generalization of the molecular representation space. A β-variational autoencoder training strategy with progressive Kullback–Leibler annealing was implemented, enabling the model to initially prioritize accurate fingerprint reconstruction before gradually enforcing latent space regularization. Here Kullback–Leibler divergence quantifies the divergence between the learned latent space probability distribution and a target standard normal distribution. The loss function integrated binary cross-entropy for fingerprint reconstruction with Kullback–Leibler divergence regularization (L_total = L_reconstruction + β × L_Kullback–Leibler), balancing effective compression and reconstruction of molecular fingerprints while fostering a smooth, well-structured latent space. Gradient clipping was applied to enhance optimization stability during training.

The DeepDrugDiscovery model demonstrated robust reconstruction performance, achieving a validation loss of 0.033 per bit, corresponding to approximately 93.3% bit-wise accuracy, and 98.9% fidelity for reference mTOR-independent autophagy enhancers, confirming effective capture of relevant molecular features (Extended Data Fig. 1c). Leave-one-out cross-validation on 50 mTOR-independent enhancers yielded a high retrieval success rate (Hit@500 = 86), with enrichment factors reaching up to 162-fold over random selection and strong ranking quality (mean reciprocal rank = 0.224, normalized discounted cumulative gain@500 = 1.30) (Supplementary Table 3 and Supplementary Methods). Further analysis of out-of-distribution molecules showed that leave-one-out performance decreased for compounds with low similarity to the training data (Hit@500 = 81% for similarity <0.3, $n = 36$; 71% for similarity <0.2, $n = 21$), while substantial enrichment over random screening (up to 288-fold) and informative ranking quality were retained, indicating generalization to remote chemical space (Supplementary Table 12 and Supplementary Methods). Five-fold scaffold-split cross-validation demonstrated reduced performance compared with in-distribution validation (Hit@500 = 80.6%), yet strong enrichment over random screening (enrichment factor@100 = 152×) and meaningful ranking quality (mean reciprocal rank = 0.212; normalized discounted cumulative gain@500 = 0.70) were maintained, supporting generalization across scaffold boundaries (Supplementary Table 13 and Supplementary Methods). Multiple biologically distinct processes—including AMPK signalling, apoptosis, CDK4, HDAC, PARP and proteasome pathways—were evaluated using the same leave-one-out validation framework and consistently achieved strong enrichment over random screening (enrichment factor@100 up to 278×), with generally robust retrieval performance, supporting the potential generalizability of the platform beyond autophagy-centric chemistry (Supplementary Table 14 and Supplementary Methods). Ablation analysis further validated the robustness of the gated recurrent unit-based fusion design, as alternative configurations reduced accuracy to 80–87% (Supplementary Table 5 and Supplementary Methods).

All compounds in the library were encoded by the encoder component of the variational autoencoder into molecular representation vectors, which served as the computational input for ligand-based virtual screening. To expedite candidate selection, we implemented a molecular attention mechanism (equations (1) and (2)) that calculates the dot product between a query vector and multiple key vectors, thereby prioritizing the most relevant molecular features. In practice, cosine distance matrix was applied in a batch-wise manner to compare molecular embeddings, generating a normalized score matrix that identified compounds most closely resembling the reference mTOR-independent autophagy enhancers. This approach facilitated efficient and precise candidate prioritization, significantly enhancing the throughput and effectiveness of the ligand-based virtual screening process.

For two sets of molecular representations q_i and k_j, each vector was processed through an activation function f(), as shown in equation (1). The molecular attention was calculated by computing the dot product of the query and key vectors ($Q_i \cdot K_j$) and normalizing it by the Euclidean norm (L2-norm) $||Q_i||||K_j||$, where a small constant ε included to prevent division by zero.

$$Q_i = \mathrm{f}(q_i),\ K_j = \mathrm{f}(k_j), \tag{1}$$

$$\text{Molecular attention}_{ij} = \frac{Q_i \cdot K_j}{||Q_i||\,||K_j|| + \varepsilon}. \tag{2}$$

The molecular attention mechanism enhanced the efficient processing of nonlinear molecular representations, significantly improving the identification of candidate drugs in ligand-based virtual screening. Leveraging parallel computing, the GPU-accelerated approach achieved exceptional computational speed, completing the analysis of a 50 × 1,155,606 similarity matrix in 0.0925 s, rendering it highly suitable for screening ultra-large compound libraries. By contrast, conventional structure-based virtual screening methods are estimated to require over 1,597 days to process a library of equivalent size. In addition, a CPU-based version of the mechanism was developed for local computing environments, offering flexibility for smaller-scale applications despite operating over 3,000 times slower than its GPU-accelerated counterpart (Extended Data Fig. 2a).

The molecular attention mechanism subsequently performed scoring, generating a 50 × 1,155,606 similarity matrix to identify mTOR-independent small molecules. From this matrix, the top 500 scoring compounds for each reference were selected. Compounds with a similarity score below 0.65 were excluded, yielding a refined library of 6,834 high-potential candidates. For visualization, t-distributed stochastic neighbor embedding (t-SNE) dimensionality reduction was applied to project the data into two components, effectively illustrating the structural diversity and distribution of the compounds (Fig. 1f). In the t-SNE plot, reference compounds were depicted as larger green dots, highlighting the library's extensive coverage of diverse chemical structures. The computational system utilized an Intel Xeon W7-3455 processor with 24 physical cores and 48 logical threads, paired with an NVIDIA GeForce RTX 4090 graphics card.

ADMET Ranker platform for ADMET and BBB permeability prediction

ADMET Ranker is an advanced graph transformer model designed to predict ADMET properties. It uses a 'Structure-Informed Pre-training and Fine-tuning' paradigm, enabling the model to first learn generalizable molecular representations from large, unlabelled datasets before specializing in specific ADMET prediction tasks. The architecture integrates three key modules: (i) a structure-informed pre-training module that leverages fragment-level feature learning and masked node prediction to identify common scaffolds and substructures; (ii) a fine-tuning module that utilizes hierarchical learning rate decay and selective re-initialization to prevent overfitting while adapting the model to specific endpoints, including BBB permeability, Caco-2 and MDCK permeability, LogD, pKa and solubility; and (iii) a feature extraction module that generates robust 'neural fingerprints' for effective use in data-limited scenarios. Together, these components enable ADMET Ranker to capture complex structure–property relationships, delivering accurate predictions across diverse ADMET tasks and significantly enhancing the efficiency of virtual screening pipelines. For BBB permeability prediction specifically, ADMET Ranker was trained and validated on a meticulously curated hybrid dataset. This dataset integrates physiologically relevant in vivo data—primarily experimentally determined LogBB values (brain-to-plasma concentration ratios) sourced from peer-reviewed literature and commercial databases—with complementary in vitro permeability data from human brain endothelial cell-based transwell assays. The platform is freely accessible at https://admet.mindrank.ai/, and methodological descriptions are available in the Supplementary Methods.

We further evaluated the predictive performance of ADMET Ranker on permeability-related assays, benchmarking it against established platforms such as ADMETlab 3.0[61], SwissADME[62], admetSAR 3.0[63] and pkCSM[64]. Performance was assessed using a comprehensive set of metrics: accuracy, area under the curve, F1-score, precision, recall, Pearson correlation coefficient (R), mean absolute error and root mean squared error. ADMET Ranker achieved competitive or superior performance across these metrics (Extended Data Fig. 2b–e). Specifically, it achieved higher accuracy (0.88–0.93), area under the curve (0.81–0.82), F1-score (0.81–0.87), precision (0.80–0.94) and recall (0.81–0.82) for Caco-2 permeability classification, MDCK efflux ratio classification and BBB efflux ratio classification. For BBB regression ADMET Ranker exhibited a strong correlation ($R = 0.796$) with low mean absolute error (0.269) and root mean squared error (0.478). The 'high confidence' subset of predictions further improved performance, particularly for BBB efflux ratio classification and MDCK efflux ratio classification, with accuracy values of 0.95 and 0.86, and area under the curve values of 0.86 for both endpoints. Although performance varied across platforms and metrics, ADMET Ranker consistently showed robust predictive accuracy for key ADMET properties, particularly BBB-related endpoints. Detailed methods and results are provided in the Supplementary Information.

In our virtual screening pipeline, BBB permeability was evaluated using ADMET Ranker. Unlike traditional approaches that rely on a single predictive model, this platform simultaneously assesses physicochemical and permeability-related properties, enabling a comprehensive evaluation. This strategy minimized false positives and improved the identification of compounds with optimal BBB permeability potential. Six key physicochemical properties were evaluated to assess BBB permeability. LogD and LogP, indicators of lipophilicity, optimized lipid solubility for membrane crossing while reducing retention in non-target tissues. Water solubility ensured sufficient dissolution in the bloodstream for effective brain delivery. Ionization constants (pKa and pKb) promoted a non-ionized state at physiological pH, facilitating passage across lipid membranes. In addition, permeability-related properties were examined using predictive models focused on BBB penetration. The Caco-2 permeability (Class) score served as an initial indicator, assigning a value of 1 to compounds exhibiting 'high permeability'. In the MDCK P-gp Efflux (Class) model, compounds classified as 'high efflux' were assigned a score of 0, reflecting reduced BBB permeability owing to active efflux; all others received a score of 1, indicating lower efflux and enhanced permeability. The BBB (Class) score evaluated penetration potential, with 'BBB^{+}' compounds assigned a value of 1, signifying the capability to cross the BBB. The BBB (Regression) score further quantified permeability likelihood, refining candidate selection (Supplementary Table 6). Finally, compounds achieving a comprehensive ADMET score of 10 were designated as top candidates for experimental validation. In total, 449 candidates from the initial 6,834 hits successfully passed all physicochemical and permeability property filters.

Antibodies and reagents

Antibodies: LC3B (Novus, NB100-2220), SQSTM1/p62, phospho-Tau (Thr231) (Abcam, ab109012 and ab151559), mTOR, phospho-mTOR (Ser2448), p70 S6 kinase, phospho-p70 S6 kinase (Ser371), phospho-4E-BP1 (Thr37/46), Tau, phospho-Tau (Thr181) (Cell Signaling Technology, 2983, 5536, 2708, 9208, 2855, 46687 and 12885), phospho-Tau (Ser202 and Thr205), phospho-Tau (Thr217) (Thermo Fisher Scientific, MN1020, 44-744), APP, C-terminal (Sigma-Aldrich, A8717), β-amyloid (BioLegend, SIG-39200), GAPDH, HRP-conjugated goat anti-rabbit IgG (H + L), HRP goat anti-mouse IgG (ABclonal, A19056, AS014 and AS003). Reagents: clevidipine, Omb, 3′,4′,7-trimethoxyquercetin, prudomestin, rhamnocitrin, ayanin, pachypodol, retusin, salicylic acid, bellidifolin, hydroxygenkwanin, prunetin, 2-HCA, riluzole, 3-hydroxycinnamic acid (MedChemExpress (Monmouth Junction), HY-17436, HY-N3139, HY-N7641, HY-N1547, HY-N1353, HY-N2913, HY-N3121, HY-N6829, HY-B0167, HY-N2000, HY-N1438, HY-N2597, HY-W012531, HY-B0211 and HY-N7127), isoamyl alcohol (Macklin, I813912), bafilomycin A_1 (Aladdin, B101389), Torin1 (LC Laboratories, T-7887), SAR405 (Sigma-Aldrich, 5330630001), DQ-Red BSA (MedChemExpress, HY-D2449), Dulbecco's modified Eagle medium, fetal bovine serum, penicillin and streptomycin antibiotics, Dulbecco's phosphate-buffered saline (PBS), BCA protein concentration assay kit (Thermo Fisher Scientific, 12100046, 10270106, 10378016, 21600010 and 23225), PVDF membrane, non-fat milk (Bio-Rad Laboratories, 1620177, 170-6404) and High Sensitivity ECL Kit (MedChemExpress (Monmouth Junction), HY-K2005).

Plasmid construction and cell line establishment

We obtained the following cDNA constructs from MiaoLingBio: mRFP-EGFP-LC3B (P4838), tau P301L (P21765), and APP K595N, M596L and V642F (P26936). These were cloned into either conventional or doxycycline-inducible lentiviral vectors using a homologous recombination kit (Beyotime Biotechnology, D7010). For the inducible vectors, gene expression was maintained with 0.5 μg ml^{-1} doxycycline. Plasmid accuracy was verified by sequencing. Lentiviruses were produced using a third-generation packaging system. Subsequently, we infected cells with these lentiviruses and established stable cell lines through puromycin or blasticidin S selection.

Pharmacokinetic study of Omb and 2-HCA in mice

The pharmacokinetic study was performed at WuXi AppTec and adhered to the study protocol and standard operating procedures (SOPs).

Animals and drug administration. Eight-week-old male CD-1 mice were housed under a 12 h/12 h light/dark cycle with free access to food and water. On the experimental day, Omb or 2-HCA was administered as a single intravenous bolus injection via the tail vein at a dose of 10 mg kg^{-1}. Omb was dissolved in a mixture of *N*-methyl-2-pyrrolidone and PEG300 (10:90, v/v), and 2-HCA was dissolved in 20% (w/v) hydroxypropyl-β-cyclodextrin aqueous solution. At 0.5 h, 1 h and 2 h post-dose, mice ($n = 3$) were anaesthetized. Blood was collected via the jugular vein puncture into K_2-EDTA-coated tubes and kept on wet ice. Plasma was obtained by centrifugation at 3,200 × *g* for 10 min at 4 °C and stored at −80 °C. Cerebrospinal fluid was collected from the cisterna magna (5 μl), transferred to low-binding tubes, flash-frozen and stored at −80 °C. Before tissue collection, animals were transcardially perfused with ice-cold saline to clear blood from the vasculature. Whole brains were excised, rinsed with cold saline, blotted dry and weighed. The right hemisphere was homogenized in methanol/15 mM

PBS (1:2, v/v) at a ratio of 1:9 (weight/volume), and about 0.8 ml tissue homogenate was stored at −80 °C. The left hemisphere was flash-frozen intact as a backup.

Sample preparation. For plasma and brain homogenate samples, protein precipitation was performed in 96-well plates. Specifically, 3 µl of plasma or 40 µl of brain homogenate was aliquoted into the plate, followed by the addition of 60 µl or 160 µl of a mixed internal standard solution (containing labetalol and tolbutamide, each at 100 ng ml^{-1} in methanol), respectively. For double blank samples, an equivalent volume of pure methanol was used instead. The mixtures were vortexed for 10 min at 800 rpm and centrifuged at 3,200 × *g* for 15 min at 4 °C. Then, 55 µl of supernatant was transferred to a new plate and centrifuged again under the same conditions before liquid chromatography-tandem mass spectrometry (LC-MS/MS) analysis. Cerebrospinal fluid samples were first mixed with an equal volume of blank plasma. A 3 µl aliquot of the mixture was then processed identically to plasma samples. All sample handling was conducted using low-binding containers to minimize analyte adsorption.

LC-MS/MS analysis. Sample concentrations were determined using a Triple Quad 6500+ operating in negative electrospray ionization and multiple reaction monitoring mode. Chromatographic separation was achieved on an ACQUITY UPLC HSS T3 column (1.8 µm, 2.1 × 50 mm) maintained at 45.0 °C. The mobile phase consisted of 0.1% formic acid in water (A) and 0.1% formic acid in acetonitrile (B) using a gradient elution (5% B at 0–0.2 min, increased linearly to 100% B by 1.0 min, held at 100% B until 1.4 min and returned to 5% B at 1.41 min, maintained until 1.6 min) at a flow rate of 0.6 ml min^{-1}. The retention times were 1.08 min for Omb, 0.832 min for 2-HCA, 0.771 min for labetalol and 1 min for tolbutamide. The multiple reaction monitoring transitions were m/z 329.10/299.00 for Omb, m/z 163.00/93.00 for 2-HCA, m/z 327.00/176.10 for labetalol and m/z 269.00/169.80 for tolbutamide. Quantification was performed using the internal standard method with calibration curves ranging from 0.500 ng ml^{-1} to 3,000 ng ml^{-1} across different matrices.

Reporting summary

Further information on research design is available in the Nature Portfolio Reporting Summary linked to this article.

Data availability

Public candidate compound dataset is available via figshare at https://figshare.com/articles/dataset/Compound_Library_for_DeepDrugDiscovery_platform/31123354. DeepDrugDiscovery web interface is available at https://deepdrugdiscovery.mindrank.ai/. ADMET prediction web interface is available at https://admet.mindrank.ai/. Source data are provided with this paper.

Code availability

Primary GitHub repository is available at https://github.com/XiangLuXiao/DeepDrugDiscovery. This repository contains the complete code for model training and inference, example datasets, tutorials, documentation on computational requirements and configurations for Docker containers or Conda environments.

References

1. GBDDF Collaborators. Estimation of the global prevalence of dementia in 2019 and forecasted prevalence in 2050: an analysis for the Global Burden of Disease Study 2019. *Lancet Public Health* **7**, e105–e125 (2022).
2. Zhang, J. et al. Recent advances in Alzheimer's disease: mechanisms, clinical trials and new drug development strategies. *Signal Transduct. Target. Ther.* **9**, 211 (2024).
3. Aman, Y. et al. Autophagy in healthy aging and disease. *Nat. Aging* **1**, 634–650 (2021).
4. Nixon, R. A. & Rubinsztein, D. C. Mechanisms of autophagy-lysosome dysfunction in neurodegenerative diseases. *Nat. Rev. Mol. Cell Biol.* **25**, 926–946 (2024).
5. Zhang, X. W. et al. Targeting autophagy in Alzheimer's disease: animal models and mechanisms. *Zool. Res.* **44**, 1132–1145 (2023).
6. Kerr, J. S. et al. Mitophagy and Alzheimer's disease: cellular and molecular mechanisms. *Trends Neurosci.* **40**, 151–166 (2017).
7. Kobro-Flatmoen, A. et al. Re-emphasizing early Alzheimer's disease pathology starting in select entorhinal neurons, with a special focus on mitophagy. *Ageing Res. Rev.* **67**, 101307 (2021).
8. Deng, Z. et al. Pharmacological modulation of autophagy for Alzheimer's disease therapy: opportunities and obstacles. *Acta Pharm. Sin. B* **12**, 1688–1706 (2022).
9. Date, Y. et al. Novel autophagy inducers by accelerating lysosomal clustering against Parkinson's disease. *eLife* **13**, e98649 (2024).
10. Sarkar, S. Regulation of autophagy by mTOR-dependent and mTOR-independent pathways: autophagy dysfunction in neurodegenerative diseases and therapeutic application of autophagy enhancers. *Biochem. Soc. Trans.* **41**, 1103–1130 (2013).
11. Dong, Y. et al. Autophagy modulator scoring system: a user-friendly tool for quantitative analysis of methodological integrity of chemical autophagy modulator studies. *Autophagy* **16**, 195–202 (2020).
12. Zhang, H. et al. Heterophyllin B enhances transcription factor EB-mediated autophagy and alleviates pyroptosis and oxidative stress after spinal cord injury. *Int. J. Biol. Sci.* **20**, 5415–5435 (2024).
13. Williams, A. et al. Novel targets for Huntington's disease in an mTOR-independent autophagy pathway. *Nat. Chem. Biol.* **4**, 295–305 (2008).
14. Zhang, X. et al. MTOR-independent, autophagic enhancer trehalose prolongs motor neuron survival and ameliorates the autophagic flux defect in a mouse model of amyotrophic lateral sclerosis. *Autophagy* **10**, 588–602 (2014).
15. Mak, K. K. et al. *Artificial intelligence in Drug Discovery and Evaluation: Safety and Pharmacokinetic Assays* (eds Franz, J. H. & Michael, K.) 1461–1498 (Springer, 2024).
16. Rehman, A. U. et al. Role of artificial intelligence in revolutionizing drug discovery. *Fundam. Res.* **5**, 2667–3258 (2024).
17. Niu, Y. Z. & Lin, P. Advances of computer-aided drug design (CADD) in the development of anti-Azheimer's-disease drugs. *Drug Discov. Today* **28**, 103665 (2023).
18. Zhou, G. et al. An artificial intelligence accelerated virtual screening platform for drug discovery. *Nat. Commun.* **15**, 7761 (2024).
19. Zhang, K. et al. Artificial intelligence in drug development. *Nat. Med.* **31**, 45–59 (2025).
20. Xiang, H. et al. Drug discovery by targeting the protein-protein interactions involved in autophagy. *Acta Pharm. Sin. B* **13**, 4373–4390 (2023).
21. Yang, X. et al. Concepts of artificial intelligence for computer-assisted drug discovery. *Chem. Rev.* **119**, 10520–10594 (2019).
22. Pham, T. H. et al. A deep learning framework for high-throughput mechanism-driven phenotype compound screening and its application to COVID-19 drug repurposing. *Nat. Mach. Intell.* **3**, 247–257 (2021).
23. Xie, C. et al. Amelioration of Alzheimer's disease pathology by mitophagy inducers identified via machine learning and a cross-species workflow. *Nat. Biomed. Eng.* **6**, 76–93 (2022).
24. Mizushima, N., Yoshimori, T. & Levine, B. Methods in mammalian autophagy research. *Cell* **140**, 313–326 (2010).
25. Tanida, I. et al. Lysosomal turnover, but not a cellular level, of endogenous LC3 is a marker for autophagy. *Autophagy* **1**, 84–91 (2005).

26. Marwaha, R. & Sharma, M. DQ-Red BSA trafficking assay in cultured cells to assess cargo delivery to lysosomes. *Bio Protoc.* **7**, e2571 (2017).
27. Dong, Y. et al. Toosendanin, a novel potent vacuolar-type H^+-translocating ATPase inhibitor, sensitizes cancer cells to chemotherapy by blocking protective autophagy. *Int. J. Biol. Sci.* **18**, 2684–2702 (2022).
28. Wang, Y. & Mandelkow, E. Tau in physiology and pathology. *Nat. Rev. Neurosci.* **17**, 5–21 (2016).
29. Jonsson, T. et al. A mutation in APP protects against Alzheimer's disease and age-related cognitive decline. *Nature* **488**, 96–99 (2012).
30. DeLoach, K. E. *Characterization of Mice Expressing APPSwe/Ind in DG, CA3 or CA1 of the Hippocampus*. MSc thesis, UC San Diego (2012).
31. Cai, Z. & Yan, L. J. Rapamycin, autophagy, and Alzheimer's disease. *J. Biochem. Pharmacol. Res.* **1**, 84–90 (2013).
32. Fang, E. F. et al. Mitophagy inhibits amyloid-beta and tau pathology and reverses cognitive deficits in models of Alzheimer's disease. *Nat. Neurosci.* **22**, 401–412 (2019).
33. Pasquier, B. SAR405, a PIK3C3/Vps34 inhibitor that prevents autophagy and synergizes with MTOR inhibition in tumor cells. *Autophagy* **11**, 725–726 (2015).
34. Yamamoto, A. et al. Bafilomycin A1 prevents maturation of autophagic vacuoles by inhibiting fusion between autophagosomes and lysosomes in rat hepatoma cell line, H-4-II-E cells. *Cell Struct. Funct.* **23**, 33–42 (1998).
35. Griffin, E. F., Caldwell, K. A. & Caldwell, G. A. Genetic and pharmacological discovery for Alzheimer's disease using *Caenorhabditis elegans*. *ACS Chem. Neurosci.* **8**, 2596–2606 (2017).
36. Cao, S. Q. et al. Chemotaxis assay for evaluation of memory-like behavior in wild-type and Alzheimer's-disease-like *C. elegans* models. *STAR Protoc.* **4**, 102250 (2023).
37. Strand, B. H. et al. Survival and years of life lost in various aetiologies of dementia, mild cognitive impairment (MCI) and subjective cognitive decline (SCD) in Norway. *PLoS ONE* **13**, e0204436 (2018).
38. Larson, E. B. et al. Survival after initial diagnosis of Alzheimer disease. *Ann. Intern. Med.* **140**, 501–509 (2004).
39. Sterniczuk, R. et al. Characterization of the 3xTg-AD mouse model of Alzheimer's disease: part 1. Circadian changes. *Brain Res.* **1348**, 139–148 (2010).
40. Sterniczuk, R. et al. Characterization of the 3xTg-AD mouse model of Alzheimer's disease: part 2. Behavioral and cognitive changes. *Brain Res.* **1348**, 149–155 (2010).
41. Michaud, F. et al. Altered firing output of VIP interneurons and early dysfunctions in CA1 hippocampal circuits in the 3xTg mouse model of Alzheimer's disease. *eLife* **13**, RP95412 (2024).
42. Park, S. et al. Distinct disruptions in CA1 and CA3 place cell function in Alzheimer's disease mice. *iScience* **28**, 111631 (2025).
43. Hussain, B., Fang, C. & Chang, J. Blood-brain barrier breakdown: an emerging biomarker of cognitive impairment in normal aging and dementia. *Front. Neurosci.* **15**, 688090 (2021).
44. Tsartsalis, S. et al. A single nuclear transcriptomic characterisation of mechanisms responsible for impaired angiogenesis and blood-brain barrier function in Alzheimer's disease. *Nat. Commun.* **15**, 2243 (2024).
45. Tsuji, A. Small molecular drug transfer across the blood-brain barrier via carrier-mediated transport systems. *NeuroRx* **2**, 54–62 (2005).
46. Ohtsuki, S. & Terasaki, T. Contribution of carrier-mediated transport systems to the blood-brain barrier as a supporting and protecting interface for the brain; importance for CNS drug discovery and development. *Pharm. Res.* **24**, 1745–1758 (2007).
47. Franken, H. et al. Thermal proteome profiling for unbiased identification of direct and indirect drug targets using multiplexed quantitative mass spectrometry. *Nat. Protoc.* **10**, 1567–1593 (2015).
48. Xie, Z. et al. Gene set knowledge discovery with Enrichr. *Curr. Protoc.* **1**, e90 (2021).
49. Tang, D. et al. SRplot: a free online platform for data visualization and graphing. *PLoS ONE* **18**, e0294236 (2023).
50. Szklarczyk, D. et al. The STRING database in 2023: protein–protein association networks and functional enrichment analyses for any sequenced genome of interest. *Nucleic Acids Res.* **51**, D638–D646 (2023).
51. Passaro, S. et al. Boltz-2: towards accurate and efficient binding affinity prediction. Preprint at https://www.biorxiv.org/content/10.1101/2025.06.14.659707v1 (2025).
52. Bhatt, P. et al. Artificial intelligence in pharmaceutical industry: revolutionizing drug development and delivery. *Curr. Artif. Intell.* **2**, E051223224198 (2024).
53. Aundhia, C. et al. Impact of artificial intelligence on drug development and delivery. *Curr. Top. Med. Chem.* **25**, 1165–1184 (2025).
54. Jung, S., Vatheuer, H. & Czodrowski, P. VSFlow: an open-source ligand-based virtual screening tool. *J. Cheminform.* **15**, 40 (2023).
55. Ni, B. et al. AutoDock-SS: AutoDock for multiconformational ligand-based virtual screening. *J. Chem. Inf. Model.* **64**, 3779–3789 (2024).
56. Cleves, A. E., Johnson, S. R. & Jain, A. N. Electrostatic-field and surface-shape similarity for virtual screening and pose prediction. *J. Comput. Aided Mol. Des.* **33**, 865–886 (2019).
57. Hawkins, P. C., Skillman, A. G. & Nicholls, A. Comparison of shape-matching and docking as virtual screening tools. *J. Med. Chem.* **50**, 74–82 (2007).
58. Yan, X. et al. Enhancing molecular shape comparison by weighted Gaussian functions. *J. Chem. Inf. Model.* **53**, 1967–1978 (2013).
59. Puertas-Martin, S. et al. OptiPharm: an evolutionary algorithm to compare shape similarity. *Sci. Rep.* **9**, 1398 (2019).
60. Ballester, P. J. & Richards, W. G. Ultrafast shape recognition to search compound databases for similar molecular shapes. *J. Comput. Chem.* **28**, 1711–1723 (2007).
61. Fu, L. et al. ADMETlab 3.0: an updated comprehensive online ADMET prediction platform enhanced with broader coverage, improved performance, API functionality and decision support. *Nucleic Acids Res.* **52**, W422–W431 (2024).
62. Daina, A., Michielin, O. & Zoete, V. SwissADME: a free web tool to evaluate pharmacokinetics, drug-likeness and medicinal chemistry friendliness of small molecules. *Sci. Rep.* **7**, 42717 (2017).
63. Gu, Y. et al. admetSAR3.0: a comprehensive platform for exploration, prediction and optimization of chemical ADMET properties. *Nucleic Acids Res.* **52**, W432–W438 (2024).
64. Pires, D. E., Blundell, T. L. & Ascher, D. B. pkCSM: predicting small-molecule pharmacokinetic and toxicity properties using graph-based signatures. *J. Med. Chem.* **58**, 4066–4072 (2015).
65. Moulis, M. & Vindis, C. Methods for measuring autophagy in mice. *Cells* **6**, 14 (2017).
66. Liu, J. & Li, L. Targeting autophagy for the treatment of Alzheimer's disease: challenges and opportunities. *Front. Mol. Neurosci.* **12**, 203 (2019).
67. Choo, M. Z. Y. & Chai, C. L. L. The polypharmacology of natural products in drug discovery and development. *Annual Reports in Medicinal Chemistry* (ed. Karl-Heinz, A.) Vol. 61, 55–100 (Elsevier, 2023).
68. Naskar, R. et al. A critical appraisal of geroprotective activities of flavonoids in terms of their bio-accessibility and polypharmacology. *Neurochem. Int.* **180**, 105859 (2024).

Acknowledgements

This study was supported by the Dr. Stanley Ho Medical Development Foundation (file number SHMDF-OIRFS/2024/002), the National Natural Science Foundation of China (number 82271455), the Science and Technology Development Fund, Macau SAR (file numbers 0040/2024/RIB1 and 0002/2025/NRP), the Guangdong Basic and Applied Basic Research Foundation (file number 2024A1515012740) and the University of Macau grants (file numbers MYRG-GRG2024-00238-ICMS-UMDF and MYRG-GRG2023-00089-ICMS-UMDF) awarded to J.-H.L. The Wellcome Leap Dynamic Resilience programme (co-funded by Temasek Trust) was awarded to X.X. and Z.N. The EPSRC Doctoral Training Programme was awarded to X.X. The ERC IMI (101005122), the H2020 (952172), the MRC (MC/PC/21013), the Royal Society (IEC\NSFC\211235), the NVIDIA Academic Hardware Grant Program, the SABER project supported by Boehringer Ingelheim Ltd., NIHR Imperial Biomedical Research Centre (RDA01), the Wellcome Leap Dynamic Resilience programme (co-funded by Temasek Trust), UKRI guarantee funding for Horizon Europe MSCA Postdoctoral Fellowships (EP/Z002206/1), UKRI MRC Research Grant, TFS Research Grants (MR/U506710/1), and the UKRI Future Leaders Fellowship (MR/V023799/1) were awarded to G.Y. We thank the members of the Faculty of Health Sciences Animal Facility at the University of Macau for their experimental and technical support. Parts of figures were created using templates from Servier Medical Art (https://smart.servier.com/), licensed under CC BY 4.0 (https://creativecommons.org/licenses/by/4.0/).

Author contributions

J.-H.L. and Z.N. conceived and supervised the project. Y.D. designed and conducted the experiments, acquired and analysed the data, and drafted the paper. X.X. and W.W. contributed to the development of AI-driven drug screening and network platform. X.-X.Z. and Z.-Y.W. contributed to the mouse and nematode experiments. S.Z. and C.S.H.T. contributed to the thermal proteome profiling. K.Z. contributed to the plasmid construction. J.-T.L., W.-Y.F., J.-M.C., S.H.X., J.-B.W. and H.Y. contributed to the LC-MS/MS analysis. S.D., K.L., C.M., W.J., X.J. and Q.C. contributed to the AI-driven drug screening and network platform. H.-M.S., H.S., M.L., D.O., K.Y., E.F.F. and G.Y. contributed to the revision of the paper. All authors reviewed, read and approved the final paper.

Competing interests

E.F.F. is a co-owner of Fang-S Consultation AS (organization number 931 410 717) and NO-Age AS (organization number 933 219 127); he has an MTA with LMITO Therapeutics Inc., a CRADA arrangement with ChromaDex, a commercialization agreement with Molecule AG/VITADAO, and MTAs with GeneHarbor (Hong Kong) Biotechnologies Limited and Hong Kong Longevity Science Laboratory; he is a consultant to MindRank AI, NYO3, AgeLab (Vitality Nordic AS) and Hong Kong Longevity Science Laboratory. Z.N., X.X., W.W., W.J., C.M., X.J., Q.C. and S.D. are employers of MindRank AI.

Additional information

Extended data is available for this paper at https://doi.org/10.1038/s41551-026-01667-x.

Supplementary information The online version contains supplementary material available at https://doi.org/10.1038/s41551-026-01667-x.

Correspondence and requests for materials should be addressed to Zhangming Niu or Jia-Hong Lu.

Peer review information *Nature Biomedical Engineering* thanks Agustín Ibáñez and Ho Ko for their contribution to the peer review of this work.

Reprints and permissions information is available at www.nature.com/reprints.

Publisher's note Springer Nature remains neutral with regard to jurisdictional claims in published maps and institutional affiliations.

Springer Nature or its licensor (e.g. a society or other partner) holds exclusive rights to this article under a publishing agreement with the author(s) or other rightsholder(s); author self-archiving of the accepted manuscript version of this article is solely governed by the terms of such publishing agreement and applicable law.

© The Author(s), under exclusive licence to Springer Nature Limited 2026

---

[1]State Key Laboratory of Mechanism and Quality of Chinese Medicine, Institute of Chinese Medical Sciences, University of Macau, Macau SAR, China. [2]Bioengineering Department and Imperial-X, Imperial College London, London, UK. [3]Mindrank AI Ltd, Hangzhou, China. [4]AI Research Center, MindRank Technologies Limited, London, UK. [5]Department of Bioinformatics and Systems Biology, Huazhong University of Science and Technology, College of Life Sciences and Technology, Wuhan, China. [6]Guangzhou National Laboratory, Guangzhou, China. [7]Interdisciplinary Institute for Personalized Medicine in Brain Disorders, School of Traditional Chinese Medicine, Jinan University, Guangzhou, China. [8]Department of Chemistry, School of Science, Southern University of Science and Technology, Shenzhen, China. [9]Department of Biomedical Sciences, Faculty of Health Sciences, Ministry of Education Frontiers Science Center for Precision Oncology, University of Macau, Macau SAR, China. [10]Mr. & Mrs. Ko Chi-Ming Centre for Parkinson's Disease Research, School of Chinese Medicine, Hong Kong Baptist University, Hong Kong SAR, China. [11]Department of Public Health and Medicinal Administration, Faculty of Health Sciences, University of Macau, Macau SAR, China. [12]Faculty of Life and Health Sciences, Shenzhen University of Advanced Technology (SUAT), Shenzhen, China. [13]Department of Clinical Molecular Biology, University of Oslo and Akershus University Hospital, Lørenskog, Norway. [14]The Norwegian Centre on Healthy Ageing (NO-Age) and the Norwegian National anti-Alzheimer's Disease (NO-AD) Networks, Oslo, Norway. [15]National Heart and Lung Institute, Imperial College London, London, UK. [16]Cardiovascular Research Centre, Royal Brompton Hospital, London, UK. [17]School of Biomedical Engineering & Imaging Sciences, King's College London, London, UK. [18]These authors contributed equally: Yu Dong, Xianglu Xiao, Xu-Xu Zhuang, Wenfan Wu. ✉e-mail: zhangming@mindrank.ai; jiahonglu@um.edu.mo

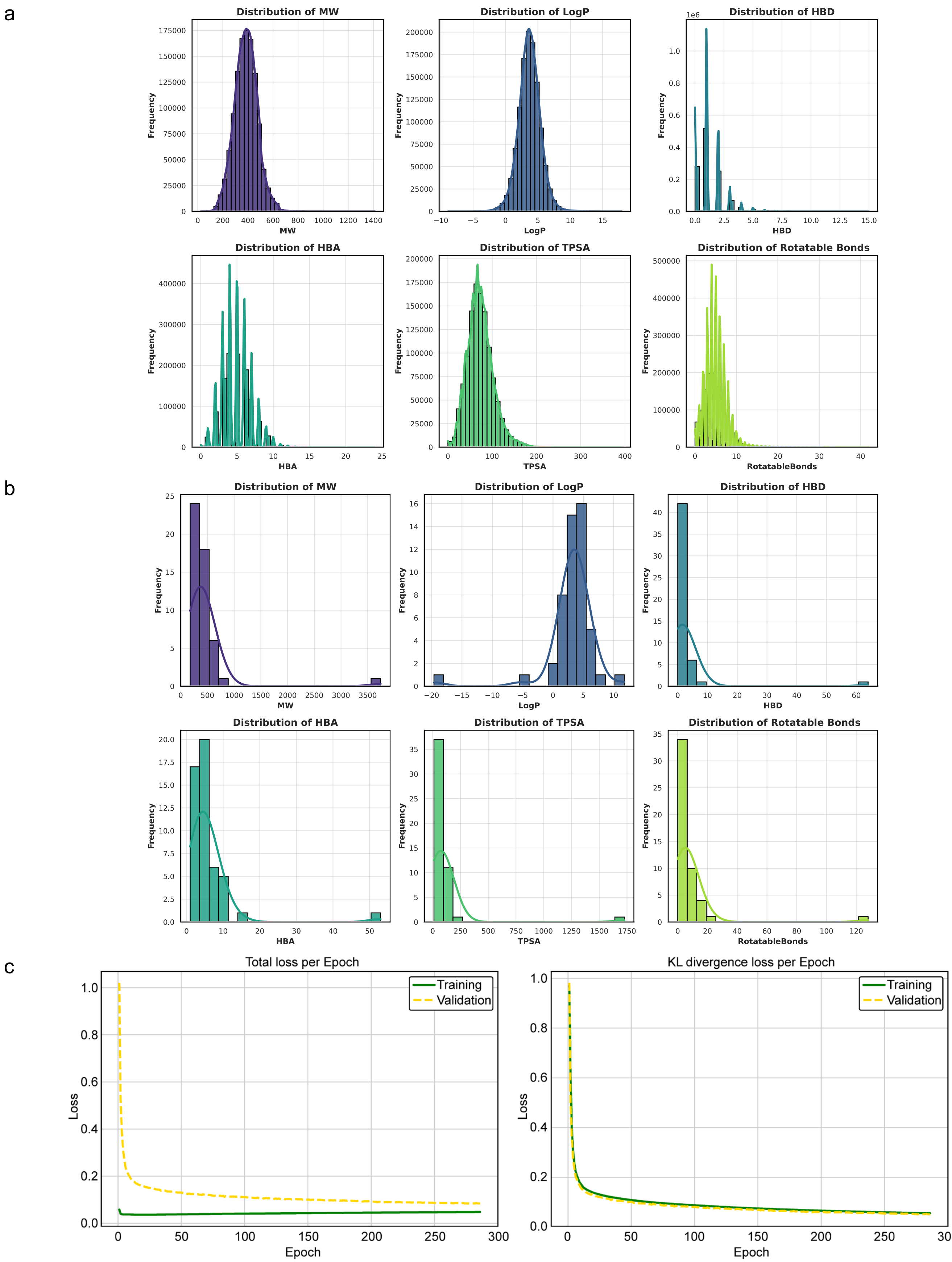

Extended Data Fig. 1 | See next page for caption.

Extended Data Fig. 1 | Physicochemical property distribution of compounds and variational autoencoder training performance. a,b, Key physicochemical and drug-likeness parameters of the virtual screening compound library and 50 reference mTOR-independent autophagy enhancers. Properties analyzed include molecular weight (MW), lipophilicity (LogP), hydrogen bond donors (HBDs), hydrogen bond acceptors (HBAs), topological polar surface area (TPSA), and rotatable bond count. **c**, Training and validation loss curves for the variational autoencoder on the DeepDrugDiscovery platform. The left panel shows the total loss (combined reconstruction and Kullback-Leibler (KL) divergence loss), and the right panel shows the Kullback-Leibler divergence loss alone.

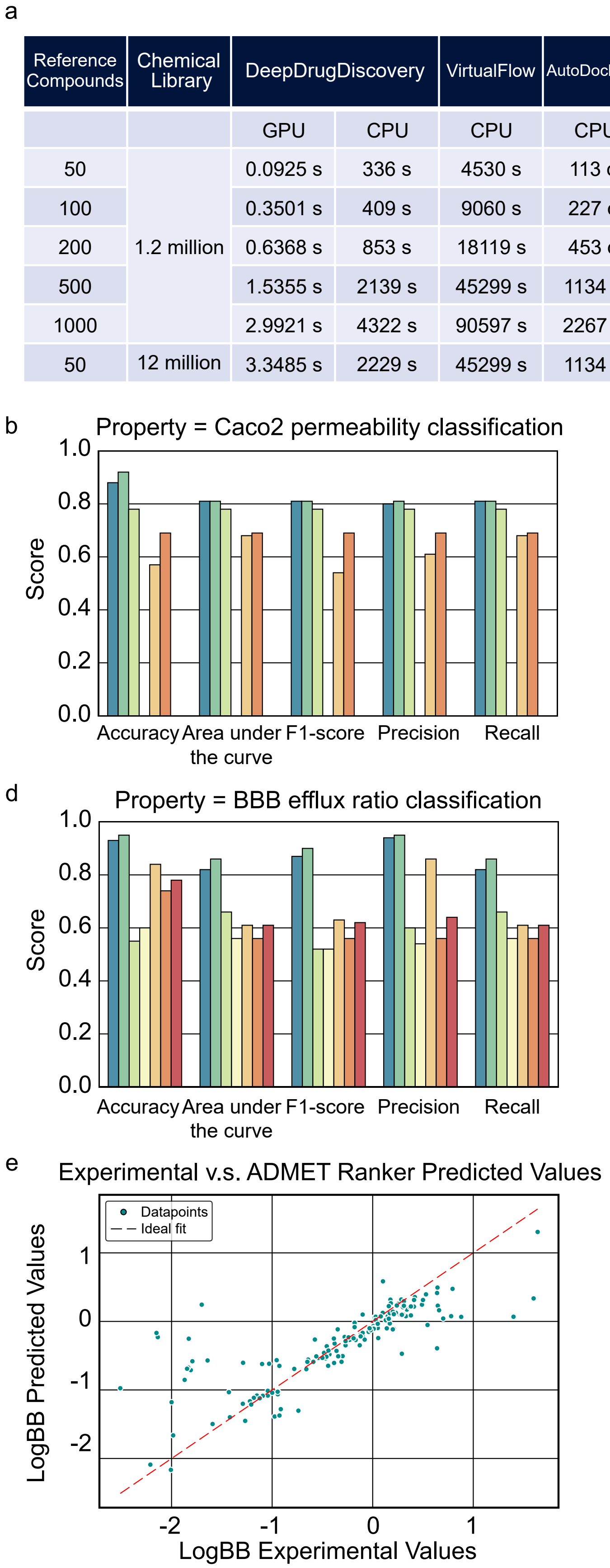

Reference Compounds	Chemical Library	DeepDrugDiscovery		VirtualFlow	AutoDock-SS	eSim-pfastf	ROCS	WEGA	OptiPharm	USR
		GPU	CPU	CPU	CPU	CPU	CPU	CPU	CPU	CPU
50	1.2 million	0.0925 s	336 s	4530 s	113 d	2 d	13 d	25 d	56 d	2.7 h
100		0.3501 s	409 s	9060 s	227 d	5 d	27 d	50 d	111 d	5.4 h
200		0.6368 s	853 s	18119 s	453 d	10 d	54 d	100 d	223 d	10.7 h
500		1.5355 s	2139 s	45299 s	1134 d	24 d	134 d	251 d	557 d	26.8 h
1000		2.9921 s	4322 s	90597 s	2267 d	49 d	268 d	501 d	1115 d	53.6 h
50	12 million	3.3485 s	2229 s	45299 s	1134 d	24 d	134 d	251 d	557 d	26.8 h

Extended Data Fig. 2 | See next page for caption.

Extended Data Fig. 2 | Benchmarking of our AI platform against public platforms. a, Comparison of computational time for DeepDrugDiscovery versus VSFlow, AutoDock-SS, eSim-pfastf, ROCS, WEGA, OptiPharm, and USR (s: seconds; h: hours; d: days). **b-d**, Comparison of Caco-2 permeability, MDCK efflux ratio, and blood-brain barrier penetration classification performance across ADMET Ranker, ADMETlab 3.0, SwissADME, admetSAR 3.0, pkCSM (Deep-PK), along with high-confidence prediction subsets from ADMET Ranker and pkCSM predictions. Performance metrics include accuracy, AUC, F1-score, precision, and recall. Missing bars indicate that a given platform does not generate predictions for the specific endpoint or metric. **e**, Scatter plot showing the correlation between experimentally derived LogBB values and the predicted blood-brain barrier penetration scores from ADMET Ranker. The dashed red line indicates the ideal correlation (predicted = experimental), and cyan circles represent individual data points (compounds).

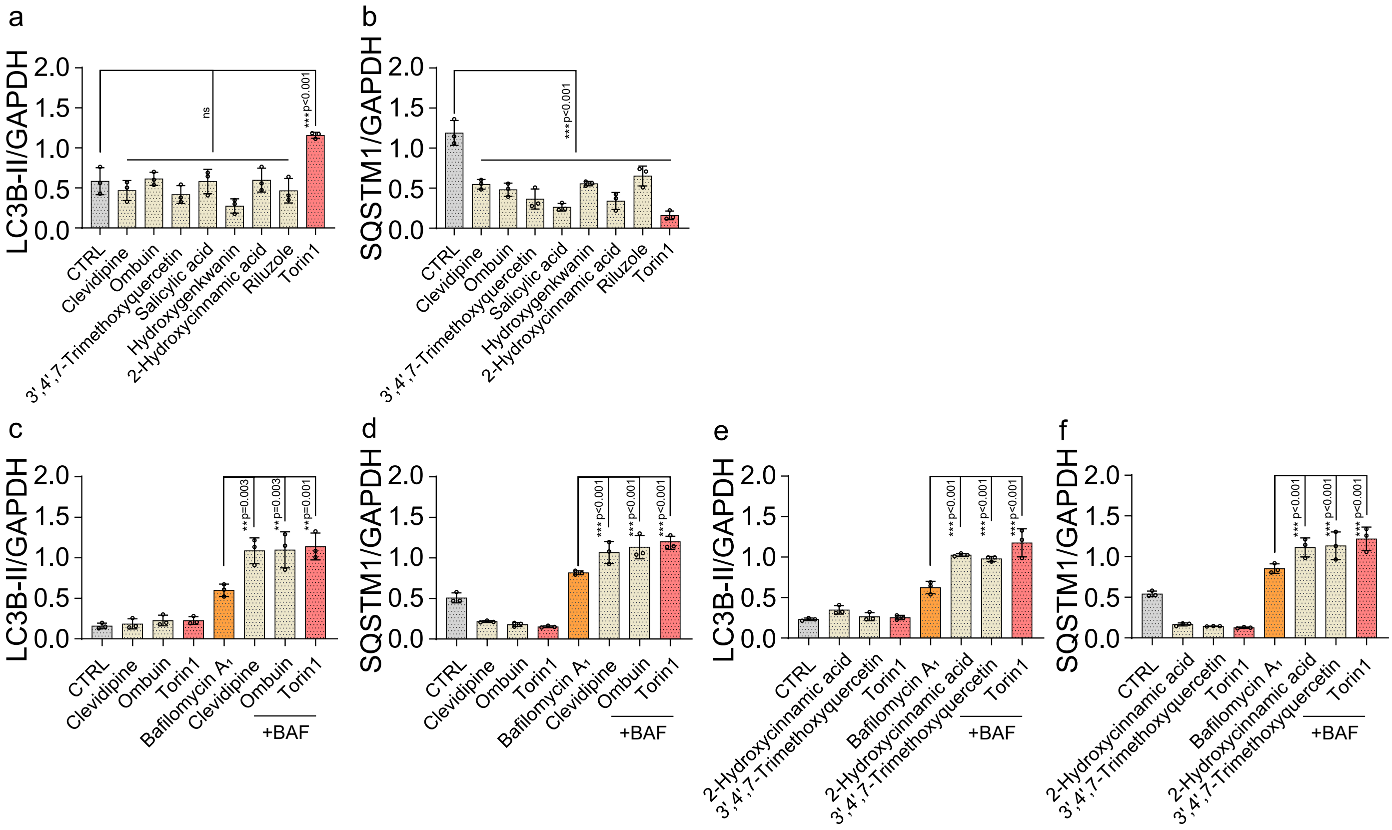

Extended Data Fig. 3 | Validation of mTOR-independent autophagy inducers. **a**,**b**, WB analysis of LC3B-II and SQSTM1/p62 protein levels in N2a cells treated with the indicated compounds (20 μM) or Torin1 (1 μM) for 24 h (n = 3 independent biological replicates). One-way ANOVA followed by Dunnett's multiple comparisons test (**a**,**b**). **c**-**f**, WB analysis of LC3B-II and SQSTM1/p62 protein levels in N2a cells treated with the indicated compounds (20 μM) or Torin1 (1 μM) in the absence or presence of Bafilomycin A_1 (100 nM) for 24 h (n = 3 independent biological replicates). One-way ANOVA followed by Tukey's multiple comparisons test (**c**-**f**). Quantitative data are shown as mean ± SD. ns, not significant, $^{*}P < 0.05$, $^{**}P < 0.01$, $^{***}P < 0.001$.

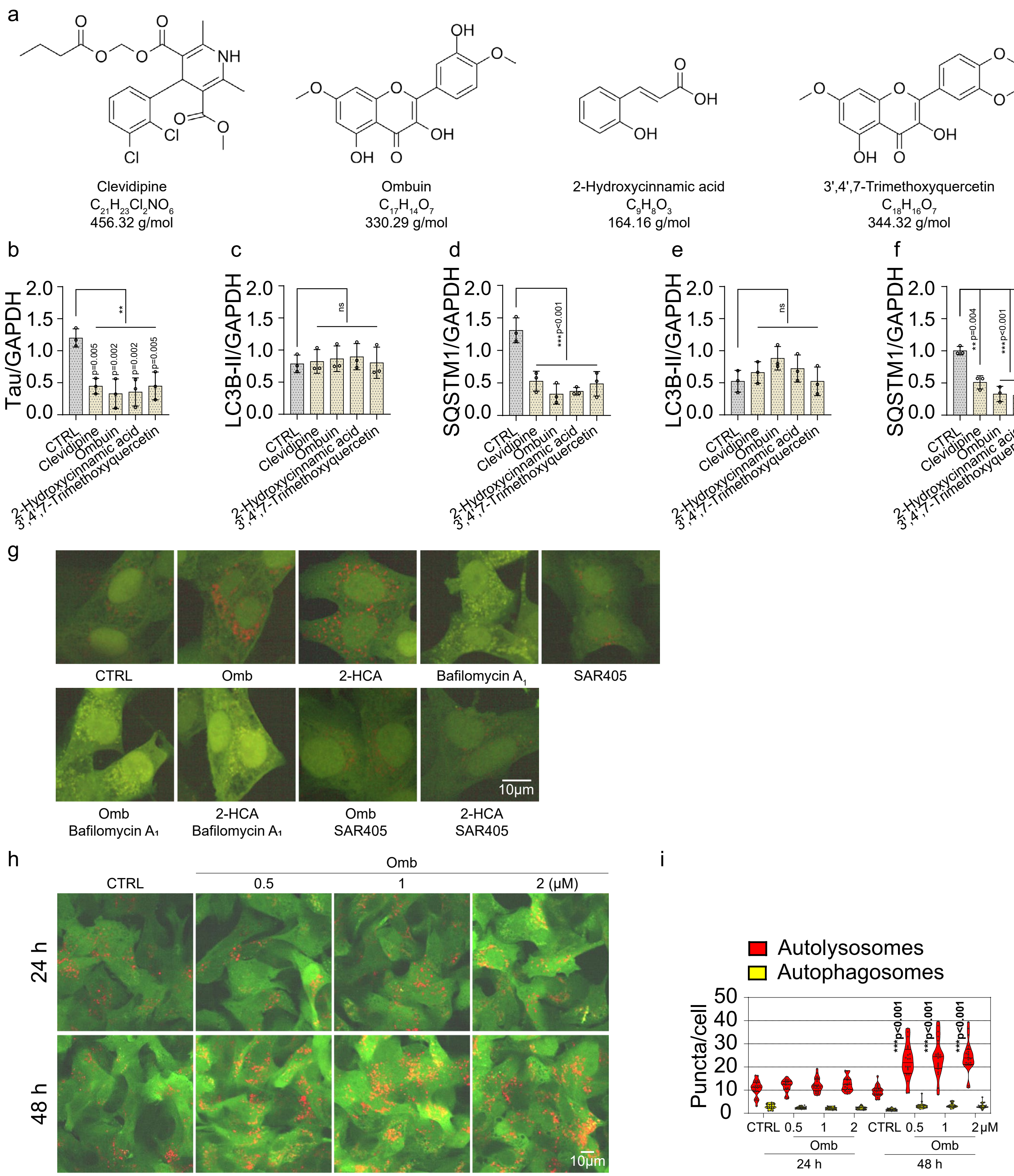

Extended Data Fig. 4 | Evaluation of abnormal protein degradation effect and autophagic flux by candidate autophagy enhancers. a, Chemical structures, molecular formulas and weights of four novel autophagy inducers. **b-f**, WB analysis of total tau, LC3B-II and SQSTM1/p62 protein levels in PC12 cells stably expressing Tau P301L or APP KM595/596NL, V642F treated with the indicated compounds (20 μM) (n = 3 independent biological replicates). **g**, PC12 cells stably expressing mRFP-EGFP-LC3B were treated with the indicated compounds (20 μM) in the absence or presence of BAF (100 nM) or SAR405 (1 μM) for 24 h, and Opera Phenix plus high-content screening system was applied to capture the fluorescent images (scale bar, 10 μm) (n = 2 independent biological replicates). **h-i**, PC12 cells stably expressing mRFP-EGFP-LC3B were treated with the indicated compound for 24 h or 48 h, and Opera Phenix plus high-content screening system was applied to capture the fluorescent images (scale bar, 10 μm). The average number of red and yellow dots per cell was quantified (cells≥30, n = 3 independent biological replicates). One-way ANOVA followed by Dunnett's multiple comparisons test (**b-f, i**). Quantitative data are shown as mean ± SD. ns, not significant, $^{*}P < 0.05$, $^{**}P < 0.01$, $^{***}P < 0.001$.

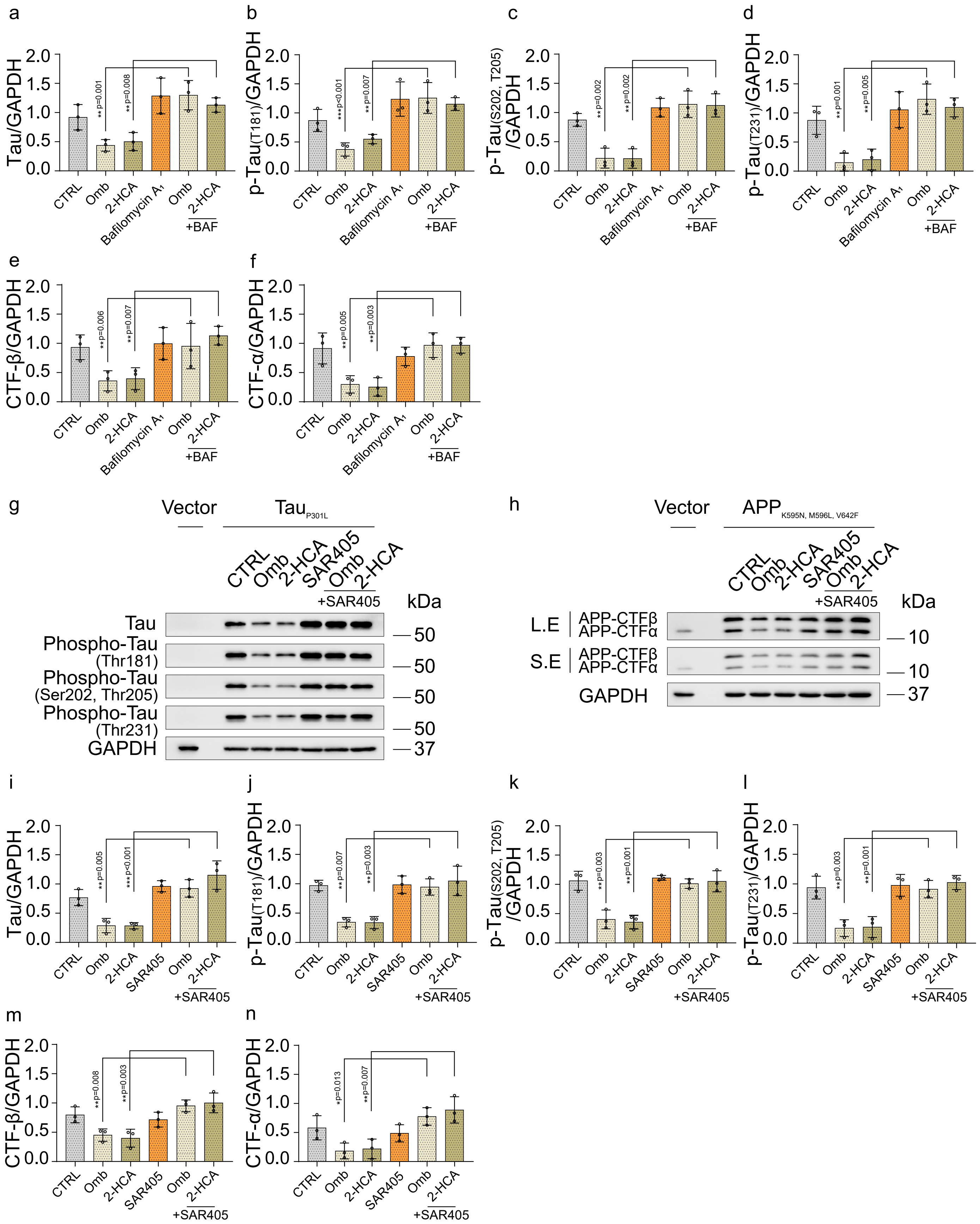

Extended Data Fig. 5 | See next page for caption.

Extended Data Fig. 5 | Ombuin and 2-Hydroxycinnamic acid clear abnormal proteins in an autophagy-dependent manner. a-n, WB analysis of total tau, phosphorylated tau (at multiple sites), CTF-β, and CTF-α protein levels in PC12 cells stably expressing Tau P301L or APP KM595/596NL, V642F treated with the indicated compounds (20 μM) in the absence or presence of BAF (100 nM) or SAR405 (1 μM) (n = 3 independent biological replicates). One-way ANOVA followed by Tukey's multiple comparisons test (**a-f, i-n**). Quantitative data are shown as mean ± SD. ns, not significant, $^{*}P < 0.05$, $^{**}P < 0.01$, $^{***}P < 0.001$. Original unprocessed WB gel data are in Source Data Fig. 6.

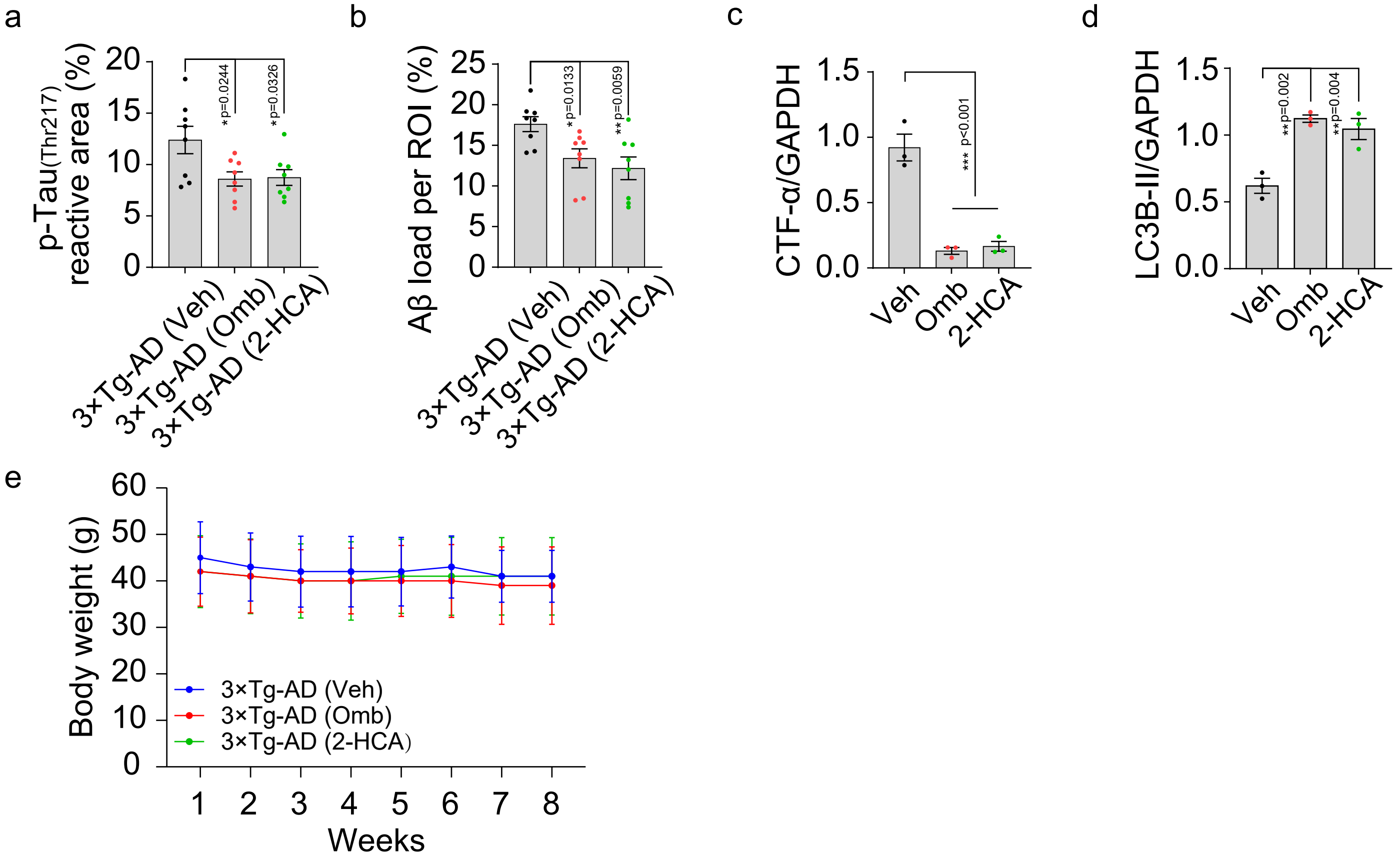

Extended Data Fig. 6 | Evaluation of the neuroprotective effects of Ombuin and 2-Hydroxycinnamic acid in the 3×Tg-AD mouse models. **a,b**, Immunofluorescence analysis of phosphorylated tau and Aβ in the hippocampal CA1 region. Relative fluorescence intensity for each treatment group was quantified (n = 7 mice per group). **c-d**, WB analysis of CTF-α and LC3B-II protein levels in mouse hippocampal tissues (n = 3 mice per group). **e**, Body weight changes in 3×Tg-AD mice throughout the treatment period (n = 7 mice per group). One-way ANOVA followed by Dunnett's multiple comparisons test (**a**-**d**). Quantitative data are shown as mean ± SD. ns, not significant, $^{*}P < 0.05$, $^{**}P < 0.01$, $^{***}P < 0.001$.

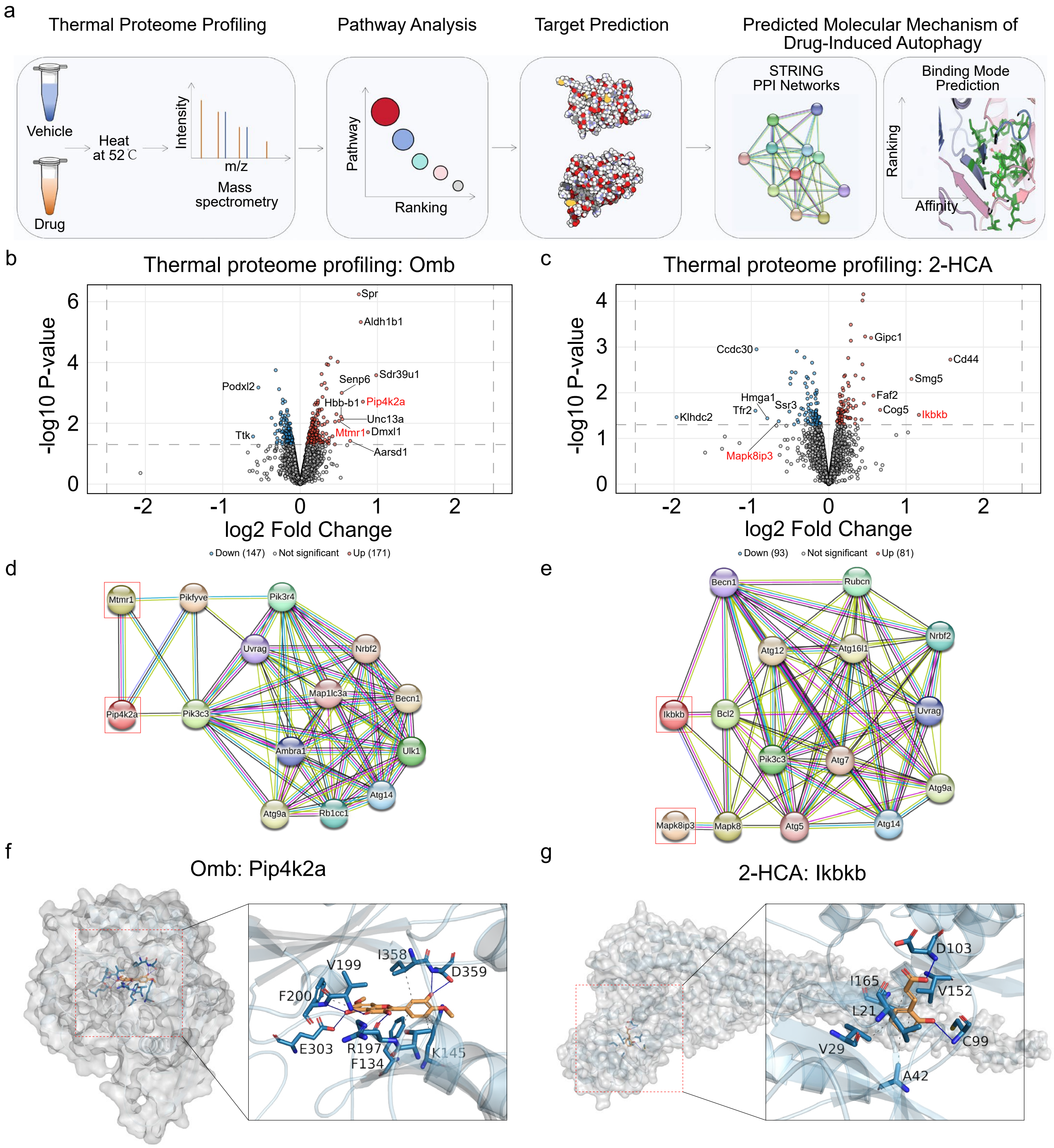

Extended Data Fig. 7 | Integrated profiling suggests candidate mechanisms for autophagy induction by Ombuin and 2-Hydroxycinnamic acid. a, Schematic workflow of the multi-faceted approach used to elucidate the mechanisms of action of the compounds. **b,c**, Thermal proteome profiling of compound-treated lysates identifies drug-binding candidates. Differential thermal stability was assessed by comparing compound-treated and vehicle-control samples using moderated t-tests implemented in the limma package (v3.62) in R. ($P < 0.05$, red dot: stabilized, blue dot: destabilized; $P < 0.05$, log2FC > 0.5, protein name: labeled). The dashed line indicates the $P = 0.05$ threshold. **d,e**, Protein-protein interaction (PPI) networks were constructed for candidate targets of Ombuin (Pip4k2a, Mtmr1) or 2-Hydroxycinnamic acid (Mapk8ip3, Ikbkb) using the STRING database to explore their coordinated roles in autophagy regulation. Edges represent predicted functional associations, colored by evidence type: purple (experimental), light blue (database), green (neighborhood), red (fusion), blue (co-occurrence), black (co-expression), light green (text mining), light purple (homology). **f,g**, Predicted binding poses for each compound-target pair, generated using the Boltz-2 deep learning method and visualized with PyMOL. Hydrogen bonds and hydrophobic interactions are indicated by blue lines and gray dashed lines, respectively.

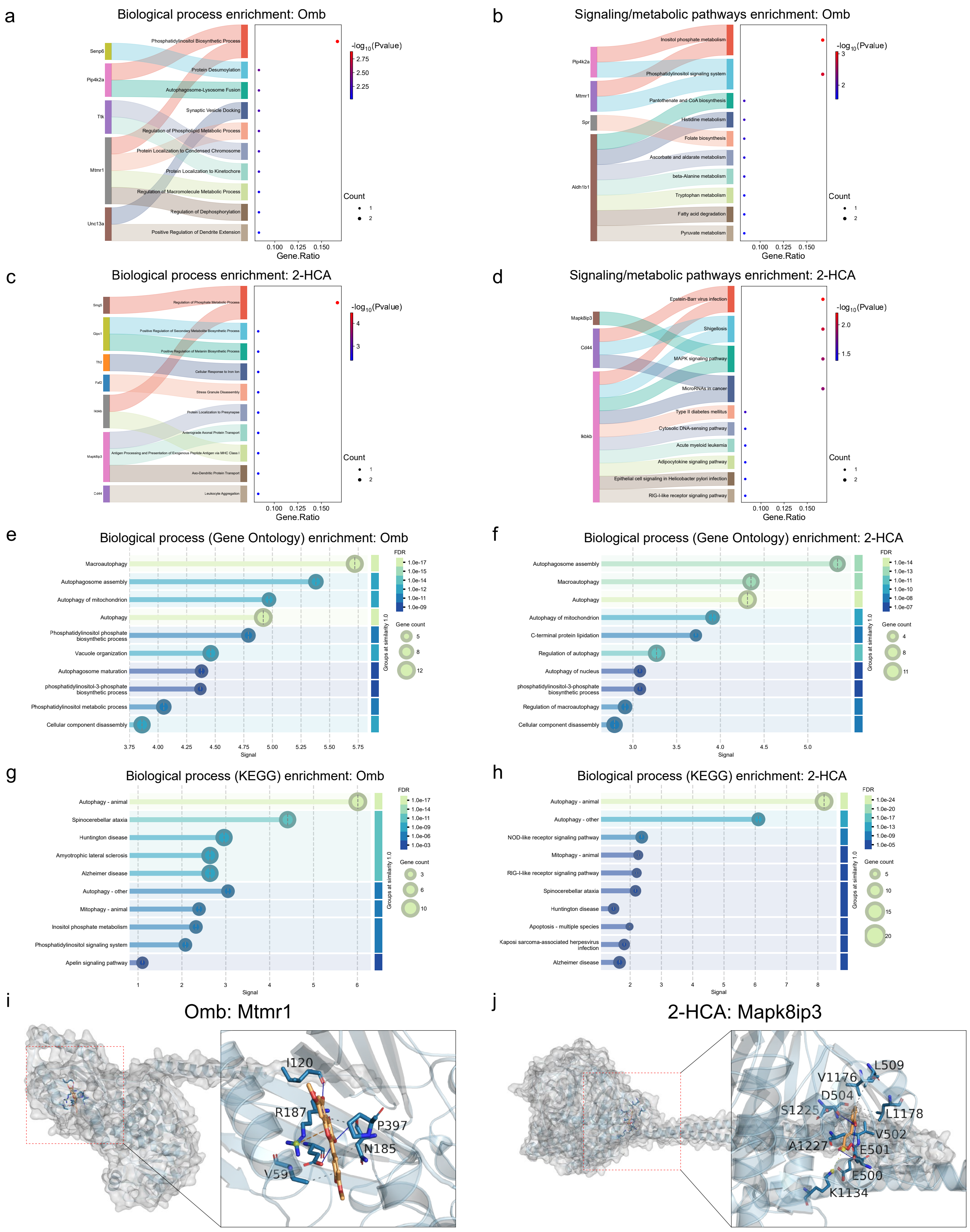

Extended Data Fig. 8 | See next page for caption.

Extended Data Fig. 8 | Integrated profiling reveals candidate mechanisms for autophagy induction by Ombuin and 2-Hydroxycinnamic acid. a-d, Integrated Sankey and dot plot illustrating the biological process and signaling/metabolic pathways (analyzed using Enrichr) associated with target proteins of Ombuin (Omb) and 2-Hydroxycinnamic acid (2-HCA), identified by thermal proteome profiling (*P* < 0.05, log2FC > 0.5). Statistical significance was determined by Fisher's exact test, and multiple testing was corrected using the Benjamini-Hochberg method. Detailed data are provided in Supplementary Tables 7–10. **e-h**, GO and KEGG enrichment analysis of the protein–protein interaction (PPI) network constructed using the STRING database for Omb and 2-HCA candidate targets, highlighting functional pathways related to autophagy regulation. **i-j**, Predicted binding poses between each compound and its target protein, generated using the Boltz-2 deep learning method and visualized with PyMOL. Hydrogen bonds and hydrophobic interactions are indicated by blue lines and gray dashed lines, respectively.

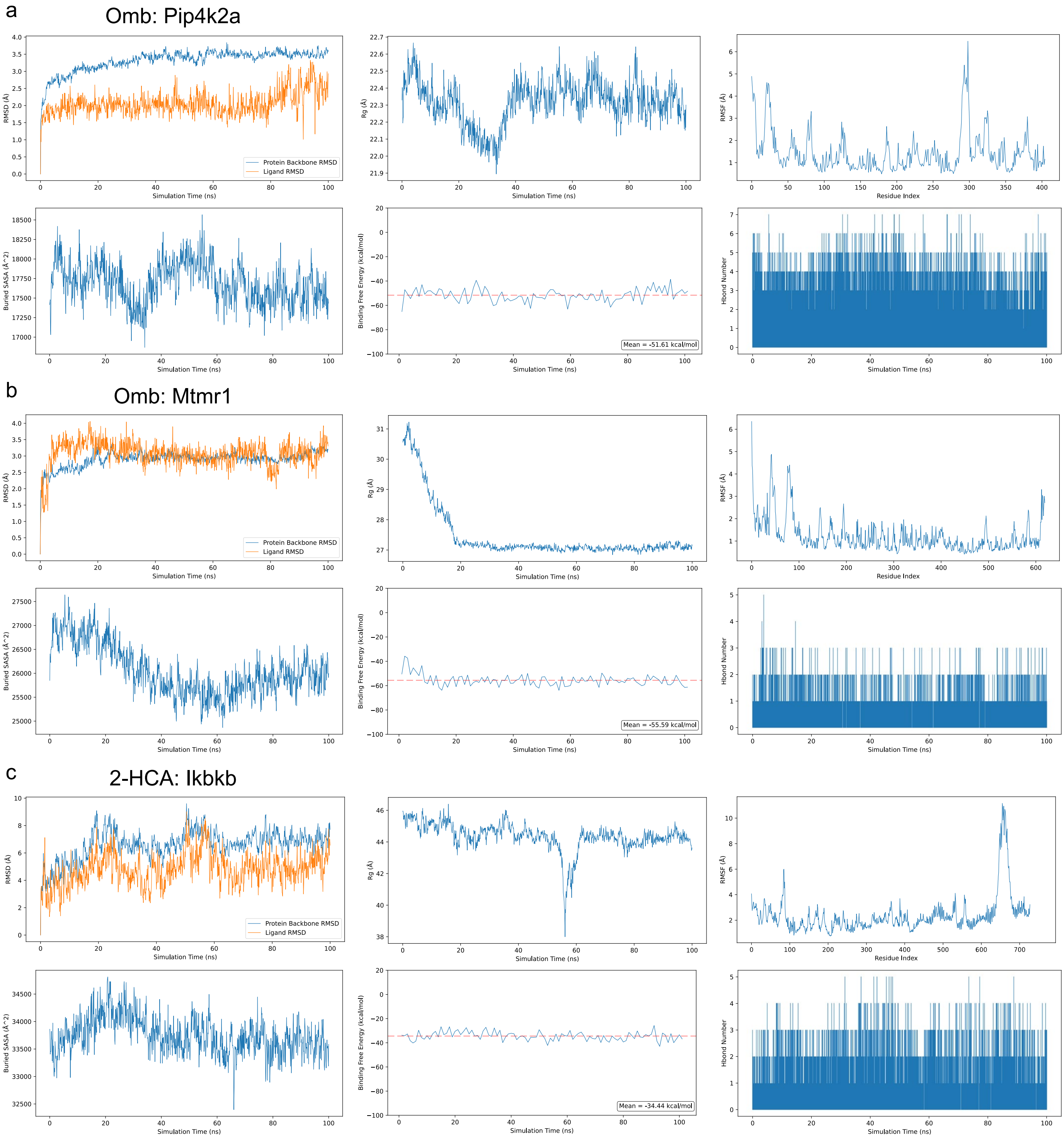

Extended Data Fig. 9 | Molecular dynamics analysis of Ombuin and 2-Hydroxycinnamic acid interactions with target proteins. a-c, Analysis plots from molecular dynamics simulations, including: (1) root mean square deviation (RMSD) of protein and ligand; (2) radius of gyration (Rg) of the complex; (3) root mean square fluctuation (RMSF) of protein residues; (4) solvent-accessible surface area (SASA) buried upon binding; (5) binding free energy; and (6) number of hydrogen bonds formed during the simulation.

nature portfolio

Corresponding author(s): Zhangming Niu, Jia-Hong Lu

Last updated by author(s): Feb 12, 2026

Reporting Summary

Nature Portfolio wishes to improve the reproducibility of the work that we publish. This form provides structure for consistency and transparency in reporting. For further information on Nature Portfolio policies, see our Editorial Policies and the Editorial Policy Checklist.

Statistics

For all statistical analyses, confirm that the following items are present in the figure legend, table legend, main text, or Methods section.

n/a	Confirmed	
☐	☒	The exact sample size (*n*) for each experimental group/condition, given as a discrete number and unit of measurement
☐	☒	A statement on whether measurements were taken from distinct samples or whether the same sample was measured repeatedly
☐	☒	The statistical test(s) used AND whether they are one- or two-sided *Only common tests should be described solely by name; describe more complex techniques in the Methods section.*
☒	☐	A description of all covariates tested
☒	☐	A description of any assumptions or corrections, such as tests of normality and adjustment for multiple comparisons
☐	☒	A full description of the statistical parameters including central tendency (e.g. means) or other basic estimates (e.g. regression coefficient) AND variation (e.g. standard deviation) or associated estimates of uncertainty (e.g. confidence intervals)
☐	☒	For null hypothesis testing, the test statistic (e.g. *F*, *t*, *r*) with confidence intervals, effect sizes, degrees of freedom and *P* value noted *Give P values as exact values whenever suitable.*
☒	☐	For Bayesian analysis, information on the choice of priors and Markov chain Monte Carlo settings
☒	☐	For hierarchical and complex designs, identification of the appropriate level for tests and full reporting of outcomes
☐	☒	Estimates of effect sizes (e.g. Cohen's *d*, Pearson's *r*), indicating how they were calculated

Our web collection on statistics for biologists contains articles on many of the points above.

Software and code

Policy information about availability of computer code

Data collection	Molecular docking was conducted using AutoDock Vina, co-folding scoring was conducted using Boltz-2, and molecular dynamics simulation was performed using the Desmond. Western Blot analysis was performed with the ChemiDoc MP system. Imaging was carried out using the IncuCyte S3 live-cell analysis system or the Leica TCS SP8 confocal laser scanning microscope system. Behavioral tracking in mice studies was performed with the Labmaze video tracking system. LC-MS/MS analysis was conducted using the Agilent Series HPLC system coupled with the AB SCIEX Triple Quad 6500 plus.
Data analysis	Data analysis was performed using GraphPad Prism 10.0. ImageJ was utilized for the analysis of Western Blot and immunofluorescence results.

For manuscripts utilizing custom algorithms or software that are central to the research but not yet described in published literature, software must be made available to editors and reviewers. We strongly encourage code deposition in a community repository (e.g. GitHub). See the Nature Portfolio guidelines for submitting code & software for further information.

Data

Policy information about availability of data

All manuscripts must include a data availability statement. This statement should provide the following information, where applicable:

- Accession codes, unique identifiers, or web links for publicly available datasets
- A description of any restrictions on data availability
- For clinical datasets or third party data, please ensure that the statement adheres to our policy

The data supporting the study's findings are presented in the paper and its supplementary materials. AI-related code and the platform used are accessible at https://github.com/XiangLuXiao/DeepDrugDiscovery, https://figshare.com/articles/dataset/Compound_Library_for_DeepDrugDiscovery_platform/31123354, and https://deepdrugdiscovery.mindrank.ai/.

Research involving human participants, their data, or biological material

Policy information about studies with human participants or human data. See also policy information about sex, gender (identity/presentation), and sexual orientation and race, ethnicity and racism.

Reporting on sex and gender	*Use the terms sex (biological attribute) and gender (shaped by social and cultural circumstances) carefully in order to avoid confusing both terms. Indicate if findings apply to only one sex or gender; describe whether sex and gender were considered in study design; whether sex and/or gender was determined based on self-reporting or assigned and methods used.* *Provide in the source data disaggregated sex and gender data, where this information has been collected, and if consent has been obtained for sharing of individual-level data; provide overall numbers in this Reporting Summary. Please state if this information has not been collected.* *Report sex- and gender-based analyses where performed, justify reasons for lack of sex- and gender-based analysis.*
Reporting on race, ethnicity, or other socially relevant groupings	*Please specify the socially constructed or socially relevant categorization variable(s) used in your manuscript and explain why they were used. Please note that such variables should not be used as proxies for other socially constructed/relevant variables (for example, race or ethnicity should not be used as a proxy for socioeconomic status).* *Provide clear definitions of the relevant terms used, how they were provided (by the participants/respondents, the researchers, or third parties), and the method(s) used to classify people into the different categories (e.g. self-report, census or administrative data, social media data, etc.)* *Please provide details about how you controlled for confounding variables in your analyses.*
Population characteristics	*Describe the covariate-relevant population characteristics of the human research participants (e.g. age, genotypic information, past and current diagnosis and treatment categories). If you filled out the behavioural & social sciences study design questions and have nothing to add here, write "See above."*
Recruitment	*Describe how participants were recruited. Outline any potential self-selection bias or other biases that may be present and how these are likely to impact results.*
Ethics oversight	*Identify the organization(s) that approved the study protocol.*

Note that full information on the approval of the study protocol must also be provided in the manuscript.

Field-specific reporting

Please select the one below that is the best fit for your research. If you are not sure, read the appropriate sections before making your selection.

☒ Life sciences ☐ Behavioural & social sciences ☐ Ecological, evolutionary & environmental sciences

For a reference copy of the document with all sections, see nature.com/documents/nr-reporting-summary-flat.pdf

Life sciences study design

All studies must disclose on these points even when the disclosure is negative.

Sample size	For experiments where statistical analysis was performed, we followed conventional experimental design principles: at least three independent biological replicates were used for cellular assays, and at least six mice were included for in vivo studies. Sample sizes for other experiments are detailed in the corresponding Methods sections or figure legends.
Data exclusions	No data were excluded.
Replication	All replication attempts were successful.
Randomization	Both nematode and mouse experiments were randomly assigned to different experimental groups.
Blinding	The researchers were blinded to animal experimental grouping and data collection.

Reporting for specific materials, systems and methods

We require information from authors about some types of materials, experimental systems and methods used in many studies. Here, indicate whether each material, system or method listed is relevant to your study. If you are not sure if a list item applies to your research, read the appropriate section before selecting a response.

Materials & experimental systems

n/a	Involved in the study	
☐	☒	Antibodies
☐	☒	Eukaryotic cell lines
☒	☐	Palaeontology and archaeology
☐	☒	Animals and other organisms
☒	☐	Clinical data
☒	☐	Dual use research of concern
☒	☐	Plants

Methods

n/a	Involved in the study	
☒	☐	ChIP-seq
☒	☐	Flow cytometry
☒	☐	MRI-based neuroimaging

Antibodies

Antibodies used	LC3B (Novus, NB100-2220), SQSTM1/p62, Phospho-Tau (Thr231) (Abcam, ab109012, ab151559), mTOR, Phospho-mTOR (Ser2448), p70 S6 Kinase, Phospho-p70 S6 Kinase (Ser371), Phospho-4E-BP1 (Thr37/46), Tau, Phospho-Tau (Thr181) (Cell Signaling Technology, 2983, 5536, 2708, 9208, 2855, 46687, 12885), Phospho-Tau (Ser202, Thr205), Phospho-Tau (Thr217) (Thermo Fisher Scientific Inc., MN1020, 44-744), Amyloid precursor protein, C-terminal (Sigma-Aldrich, A8717), β-Amyloid (Biolegend, SIG-39200), GAPDH, HRP-conjugated Goat anti-Rabbit IgG (H+L) (ABclonal, A19056, AS014).
Validation	All antibodies were validated for use in cell and mouse tissues, as supported by prior publications (Cai Cui-Zan et al., Autophagy 2021; Cai Cui-Zan et al., Theranostics 2022; Dong Yu et al., International Journal of Biological Sciences 2022; Xie Chenglong et al., Nature Biomedical Engineering 2022). Detailed antibody validation profiles are available on the respective antibody providers' websites.

Eukaryotic cell lines

Policy information about cell lines and Sex and Gender in Research

Cell line source(s)	PC12 and N2a cells, sourced from ATCC, PC12 were further engineered to overexpress mRFP-EGFP-LC3B, Tau P301L, or APP K595N, M596L, V642F.
Authentication	None of the cell lines used were authenticated.
Mycoplasma contamination	All cell lines were confirmed to be free of mycoplasma contamination.
Commonly misidentified lines (See ICLAC register)	No commonly misidentified cell lines were used.

Animals and other research organisms

Policy information about studies involving animals; ARRIVE guidelines recommended for reporting animal research, and Sex and Gender in Research

Laboratory animals	3xTg-AD mice, maintained on a B6;129 genetic background (Stock No. 004807; B6;129-Tg(APPSwe,tauP301L)1Lfa Psen1tm1Mpm/Mmjax; https://www.jax.org/strain/004807), were obtained from The Jackson Laboratory. C57BL/6J mice served as wild-type controls. All animals were housed in individually ventilated cages with standardized rodent bedding under a consistent 12-hour light/dark cycle, with ad libitum access to food and water. Sixteen-month-old female 3xTg-AD mice underwent two months of drug treatment via intraperitoneal injection, followed by behavioral and biochemical assessments.
Wild animals	The study did not involve wild animals.
Reporting on sex	Research indicates that female 3xTg-AD mice exhibit more pronounced Aβ pathology and behavioral deficits, particularly in Aβ burden and associated behavioral test performance. Carroll, Jenna C., et al. "Sex differences in β-amyloid accumulation in 3xTg-AD mice: role of neonatal sex steroid hormone exposure." Brain research 1366 (2010): 233-245. Arsenault, Dany, et al. "Sex-dependent alterations in the physiology of entorhinal cortex neurons in old heterozygous 3xTg-AD mice." Biology of sex Differences 11 (2020): 1-19. Dennison, Jessica L., et al. "Sexual dimorphism in the 3xTg-AD mouse model and its impact on pre-clinical research." Journal of Alzheimer's disease 80.1 (2021): 41-52.
Field-collected samples	The study did not involve samples collected from the field.
Ethics oversight	The Animal Ethics Application for Research was approved by the University of Macau (UMARE-046-2024).

Note that full information on the approval of the study protocol must also be provided in the manuscript.

Plants

Seed stocks	*Report on the source of all seed stocks or other plant material used. If applicable, state the seed stock centre and catalogue number. If plant specimens were collected from the field, describe the collection location, date and sampling procedures.*
Novel plant genotypes	*Describe the methods by which all novel plant genotypes were produced. This includes those generated by transgenic approaches, gene editing, chemical/radiation-based mutagenesis and hybridization. For transgenic lines, describe the transformation method, the number of independent lines analyzed and the generation upon which experiments were performed. For gene-edited lines, describe the editor used, the endogenous sequence targeted for editing, the targeting guide RNA sequence (if applicable) and how the editor was applied.*
Authentication	*Describe any authentication procedures for each seed stock used or novel genotype generated. Describe any experiments used to assess the effect of a mutation and, where applicable, how potential secondary effects (e.g. second site T-DNA insertions, mosiacism, off-target gene editing) were examined.*